ABSTRACT

Title of dissertation: CHARACTERIZING THE COMBINED EFFECT OF ELECTROSTATICS AND POLYMER ADHESION FOR ELASTOMER-BASED ELECTROADHESIVES

Simpson Abraham Chen, Doctor of Philosophy

Dissertation directed by: Professor Sarah Bergbreiter
Department of Mechanical Engineering

This dissertation presents work done in the fabrication and characterization of polymer-based electroadhesives to understand the underlying mechanisms of electroadhesion with the inclusion of soft polymers as the functional surface material. Electrostatic models for parallel plate and interdigitated electrodes provide insight into the effect of design parameters on electric fields. However, little work has been done to model how electrostatic force affect adhesion in soft electroadhesives while accounting for their mechanical and material properties.

To this end, a basic friction model is presented to describe the critical shear force for a single electrode electroadhesive. The effect of voltage, contact area, dielectric thickness, and bulk thickness on shear adhesion is explored. It was shown that within a range of design parameters the basic friction model could accurately predict the critical shear force and with stiff dielectric layers higher compliance improved adhesion. However, improved models are required to cover behavior over a larger parameter space.

To move beyond friction-based modeling, the combined effect of polymer adhesion and electrostatic force on conductive polymer layers is explored through performing JKR tack tests. Tack tests can measure the intrinsic adhesive property of a

polymer, called the critical energy release rate. By performing JKR tack tests with two different tack systems, a rigid probe contacting a soft elastic surface and a soft probe contacting a rigid surface, it was shown that the combination of the two adhesion mechanisms can be described as a superposition of the critical energy release rate of the polymer and electrostatic force.

Using these findings, a design framework is developed to combine gecko adhesives with electrostatics to increase the controllable adhesion range. Textured electroadhesives with arrays of spherical bumps were fabricated and showed an increase in adhesion up to 20x. The textured electroadhesives were also mounted onto 3D printed mounts to pick up various objects weighing from 2 g to 60 g. The work presented here provides a theoretical and design framework for future soft electroadhesives to build upon for applications from climbing robots to pick and place manufacturing.

CHARACTERIZING THE COMBINED EFFECT OF ELECTROSTATICS AND POLYMER ADHESION FOR ELASTOMER-BASED ELECTROADHESIVES

by

Simpson Abraham Chen

Dissertation submitted to the Faculty of the Graduate School of the
University of Maryland, College Park in partial fulfillment
of the requirements for the degree of
Doctor of Philosophy
2018

Advisory Committee:
Associate Professor Sarah Bergbreiter, Advisor
Professor Miao Yu
Professor Don DeVoe
Assistant Professor Siddhartha Das
Professor Pamela Abshire
Professor Alfred Crosby

Acknowledgments

There are many people who deserve thanks for their aid and support during my time as a Ph.D student. First and foremost, I would like to thank my advisor, Professor Sarah Bergbreiter. I would not have been able to complete this work if it was not for her full support and guidance throughout the years. I would also like to thank Professor Al Crosby for all his insights and advice in the field of soft polymers and adhesion, along with his graduate student Chris Barney.

I would like to thank the staff at the Maryland Nanocenter Fablab for always answering my questions and coming up with new and wild solutions for all my fabrication problems.

I would like to thank Ivan Penskiy, Ryan St. Pierre, Hee Sup Shin, and all the former labmembers at the Microrobotics Laboratory for all their feedbacks, ideas, collaborations, and conversations. Lastly, I would like to thank my parents and my wife for constantly supporting me with daily lunches and chocolates.

Table of Contents

List of Figures

Chapter 1

Introduction

Electroadhesives are capable of actively adjusting adhesion with voltage, enabling a new method for creating tunable adhesives with applications from robotics to the medical field. The focus of this dissertation addresses one of the main challenges related to electroadhesives, namely modeling and characterizing electroadhesives that use soft polymers as the functional surface. Understanding the effects of soft polymers on the performance of electroadhesives will inform design and material selection for future applications.

1.1 Adhesives

Glue, tape, permanent magnets are all common items that function to permanently or temporarily bond surfaces together. There have been many types of adhesive mechanisms developed for a wide variety of applications. There are mechanisms based on vacuum suction [5, 6], magnetics [7–9], sticky viscoelastic polymers [10, 11], and most recently, gecko-inspired adhesives that use van der Waals to stick [12–15]. Vacuum suction can be unwieldy and heavy, and electromagnets typically require large power draw. On the other hand viscoelastic polymers, most commonly used in tapes, and gecko adhesives require little to no power to achieve adhesion. A common characteristic of tapes and gecko adhesives is that they have set adhesion

strengths, defined as the force required to break contact, or tack force. The tack force, particularly along the adhesive's loading direction cannot be actively controlled and is largely dependent on the material's stiffness, the polymer's surface properties, functional surface design, and fibrillar design [16–19].

For applications in keeping two bodies permanently or temporarily attached, modulating the adhesive's strength is not as important as being sufficiently strong. However, there are cases in which it is favorable to be able to actively adjust the tack force. For climbing robots, if the payload exceeds its adhesion strength, a new adhesive needs to be fabricated and installed on the robot to accommodate for the larger payload. A tunable adhesive could be used to increase the tack force without fabricating a new device. Underactuated walking robots could use tunable adhesives at the interface of their feet and surface to improve walking efficiency or provide directional movement [20]. Electroadhesives could also be used to replace medicinal tapes. Medicinal tapes that hold IV lines to patients need significant force to remove because they are required to securely bond to the skin. The force to remove these tapes can be traumatic and cause scarring [10, 21]. Being able to actively turn "off" the tape's adhesion could solve that problem. Electroadhesives have the opportunity to capitalize on these shortcomings because they have the ability to adjust their adhesion strength with an applied voltage.

Electroadhesives have been used for climbing robots [13, 14, 22, 23], clutches for human gait assistance [24], and grasping [1, 25–27], Fig. 1.1. For climbing and grasping the electroadhesive is typically made of a thin flexible plastic with embedded electrodes, shown in Fig. 1.1B. The dielectric layer in these adhesives is on order

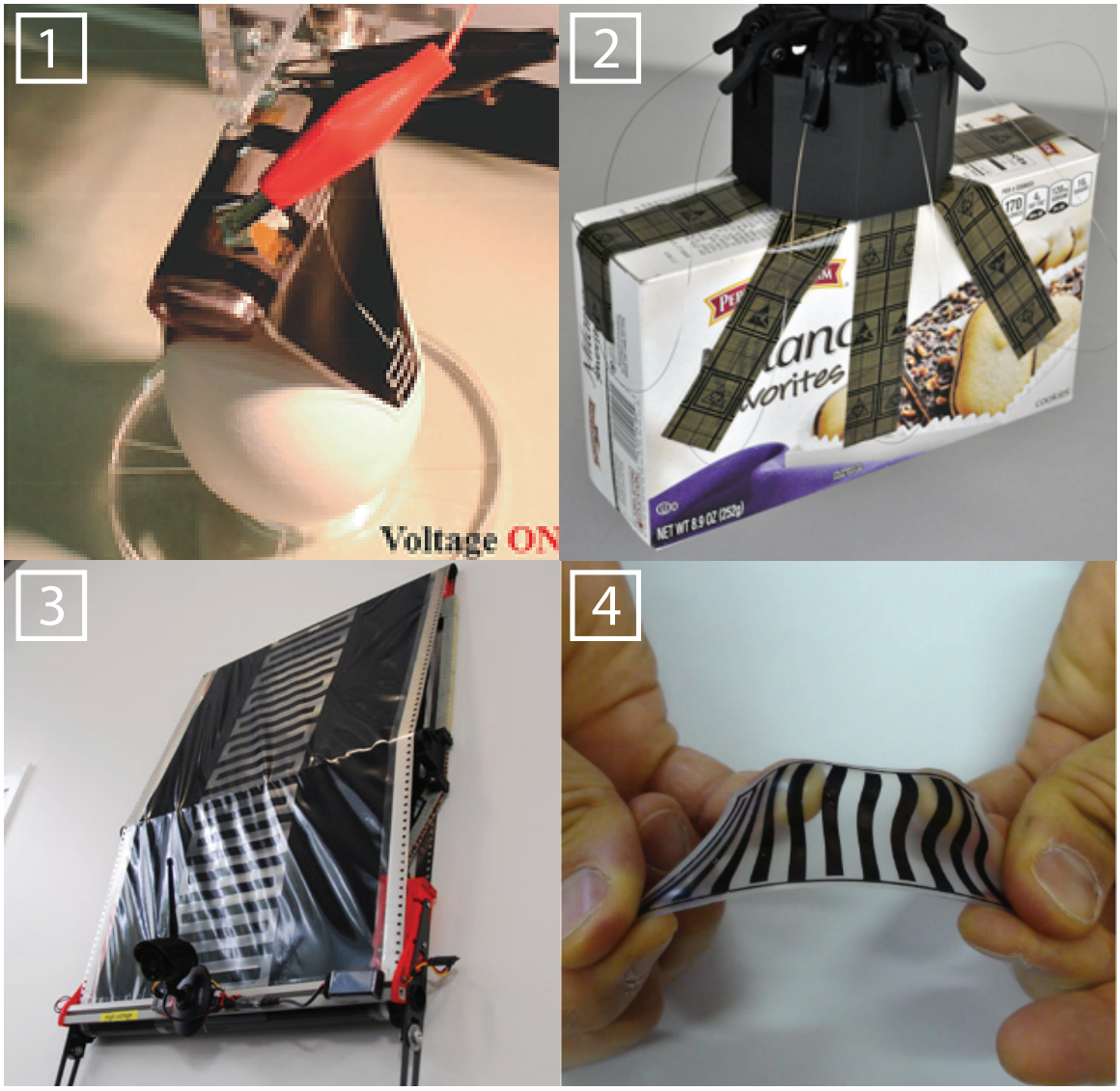

Figure 1.1: Examples of electroadhesives. 1) Electroadhesive gripper made of soft stretchable polymers from Shintake et al. [1]. 2) A electroadhesive gripper made of thin flexible plastic with embedded metal from Grabit [2]. 3) A climbing robot that uses interdigitated electrodes embedded into a plastic tread to adhere to vertical surfaces, from SRI [3]. 4) A stretchable interdigitated electroadhesives made by Germann et al. [4].

of tens of microns thick which requires applying several kilovolts to obtain sufficient adhesion. While several kilovolts are needed to achieve adhesion, it is with low current, so the power consumption is small. However, this can be difficult to implement on centimeter-scale robots since high voltages require additional circuitry and high

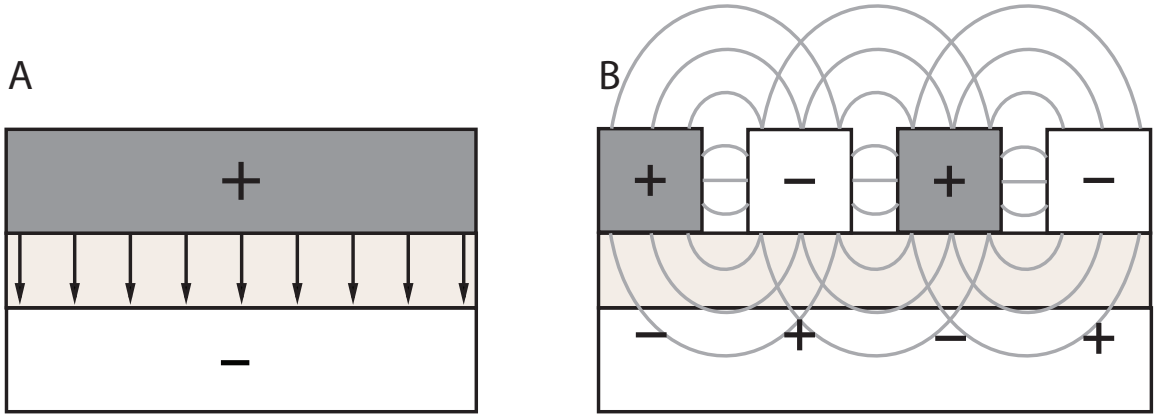

Figure 1.2: Diagram of parallel plate (A) and interdigitated electrodes (B) for electroadhesion. The plus and minus sign indicate the electrodes that are attached to the voltage source and the light gray layer is the dielectric. The lines indicate the electric fields generated by the voltage potential.

voltage converters. Most electroadhesives are built to sustain only shear forces since the thin flexible material easily peels when a normal force is applied.

Two conductive surfaces separated by a dielectric is the most basic form of an electroadhesive, shown in Fig. 1.2A. The adhesion force increases the normal load between the plates, thereby increasing the frictional force needed to detach the plates in shear. This has been used in some applications such as an electrostatic clutch or for turning in small-legged robots [20, 24]. However the parallel plate configuration requires connecting the attachment surface to the voltage source, which is impractical for applications in climbing and grasping. Rather, the interdigitated electrode design, shown in Fig. 1.2B, is more commonly used in electroadhesion. This design allows for both electrodes to be fabricated within the same substrate. By applying a voltage between the electrodes, the fringing fields induce charge on the attachment surface which induces adhesion on both conductive and non-conductive surfaces.

1.2 Soft Electroadhesives

Traditionally, electroadhesion was utilized in rigid electrostatic chucks to pick up silicon wafers [28] or flexible but non-stretchable plastic for climbing robots [13,14,22,23]. However, in recent years, researchers have taken insights from gecko-inspired adhesives to develop flexible and stretchable devices. Low modulus polymers are used because their compliant nature allows for better conformity to irregular and rough surfaces. Compliant elastomers embedded with a nickel-copper mesh were demonstrated to adhere to a variety of surfaces including cloth and floor tiles [27]. Stretchable elastomer-based electroadhesives were fabricated and were capable of shear adhesion while under a pre-strain up to 120% [4]. The authors developed a polymer-based electroadhesive with sub-micron dielectric thicknesses which obtained shear pressures up to 80 kPa on glass at 200 V [29].

While work has been done to develop soft electroadhesives, they have not yet been well characterized based on design parameters, and are rarely compared directly to theory. Ruffato et al. experimentally optimized the layout of interdigitated electrodes and found that it qualitatively matched results from finite element simulations [26]. Tellez investigated the relationship between shear adhesion to dielectric thickness and voltage for their elastomer-based electroadhesive [30]. They compared their results to the standard electrostatic force equation for parallel plates and found that shear adhesion varied linearly with applied voltage, which is inconsistent with the parallel plate equation, which states that force scales quadratically with voltage. Developing a model will help identify how compliant materials affect shear adhesion

and estimate the tack force based on design parameters.

1.3 Energy release rate

Soft polymers have adhesive properties that originate from how their molecular interface interacts with the attachment surface. Their intrinsic material properties (surface energy, elastic modulus, and viscoelastic properties) greatly influence how the interface fractures. To develop electroadhesives that use soft polymers, it is crucial to understand how polymer adhesion and electrostatic force combine to affect fracture. However, the combination of these two adhesive forces has not been thoroughly investigated.

There have been devices that use both dry fibrillar adhesives (gecko adhesives) and electroadhesion to stick [27, 31, 32]. In [27], it was found that the hybrid device extended the range of materials and roughness that adhesion can be useful. Recently, Izadi et al. found that electrostatic force potentially plays a larger role in gecko adhesion than previously thought [33, 34]. Charge on gecko adhesives can build up due to contact electrification. However, more work needs to be done to understand how the combination of the two mechanisms affects adhesion, and the current practice of measuring tack force is not sufficient for understanding the underlying contact mechanics.

Tack force depends on the stress distribution of the peeling front. It does not give the true driving force required to cause cracks to propagate. The driving force for interfacial fracture, also called critical energy release rate (G_c), is a measure of

how the molecular interface interacts with the attachment surface. It is independent of experimental conditions therefore its interfacial strength can be generalized to all systems. Performing tack tests will also provide important insight on the speed of crack propagation and can be used to obtain the characteristic crack speed, v^*. The characteristic crack speed and the critical energy release rate can be used to predict deformation mechanisms and adhesion strength in different systems [35–38]. The contact equation from Johnson, Kendall, and Roberts (JKR) is used to estimate the energy release rate of soft polymers [39]. Describing electroadhesion in terms of its effect on the energy release rate in a soft polymer system will give insights on how it affects fracture mechanics.

1.4 Dry and Electroadhesives

Currently, gecko adhesives are limited by the fixed stickiness of their surface and difficulty in scaling [40]. They have no ability to increase or decrease the adhesion of their surface; once attached, they can only turn it "off" through their detachment mechanism. Their adhesion also does not scale easily in overall device size because of difficulty in aligning fibrillar arrays and engaging all fibers during the preloading stage [40].

Electroadhesion can be quickly adjusted by varying the applied voltage. Additionally, electrostatic force can provide an electrical preload to improve contact, which may help improve the scaling of dry adheisves. By combining dry and electroadhesives, it is possible to increase the maximum adhesion force, improve contact,

and give the ability to tune the stickiness of the device.

There has been some work done to combine the two adhesive mechanisms [27, 32, 41–43]. In Ruffatto, their device has a fribillar layer for dry adhesion and a backing layer with electrodes that apply electrostatic force [27, 41]. Krahn also uses a similar stacking method in their electroadhesive device [43]. These papers have demonstrated that the electrostatic layer provides an additional electrical preload to increase contact between the surface and the dry adhesive layer. Ruffatto demonstrated that this increased the maximum load their device can hold on rough surfaces by up to 5x greater. Though on smooth surfaces such as glass and metal, the benefit of electroadhesion was not significant and improved adhesion up to 1.1x [27]. The work done to integrate soft electroadhesives and dry adhesion resulted in applied voltages in the thousands due to this stacking method. The dry adhesive layers are usually tens of microns thick which subsequently requires thousands of volts to generate sufficient force. To develop better soft electroadhesives with lower voltage requirements and a higher range of controllable adhesion, changes in the fabrication and design of the adhesive should be investigated.

1.5 Outline of Proposal

The proposal is divided into three chapters: a basic friction model for shear adhesion, characterizing electroadhesion in terms of energy release rate, and developing a design framework that combines dry and electroadhesion for a larger controllable adhesion range.

Chapter 2 presents a basic friction model to estimate the critical shear strength of an all-polymer electroadhesives based on design parameters, and is largely based on the work published in [44]. This chapter also discuss the effects of compliance on the adhesion, which is not predicted by the friction model. Chapter 3 characterizes electrostatic force in terms of energy release rate for two different probe tests. It also hypothesizes that the energy release rate from polymer adhesion and electrostatic force are independent, and that the total energy release rate, for a system where the two mechanisms exists, is a superposition of the individual forces. Chapter 4 presents a design framework to combine dry and electroadhesion while maximizing the range of forces that can be actively controlled by electrostatics. Chapter 5 summarize the results of this work.

Chapter 2

Modeling non-patterned

2.1 Introduction

A majority of the work in this chapter is taken from "A comparison of critical shear force in low-voltage, all-polymer electroadhesives to a basic friction model" [44].

The work presented in this chapter compares a basic friction model to the adhesion of polymer-based electroadhesives due to electrostatic force. This chapter examines how adhesion in shear is affected by electrostatic parameters such as the applied voltage, dielectric thickness, and contact area. It also explores how the complianace of the soft polymer contributed to viscoelastic effects that influenced adhesion not predicted by the friction model.

Electroadhesion uses an applied electric field to generate electrostatic force between surfaces, offering a simple method to control adhesion. However, electroadhesives have not yet been well characterized based on design parameters and are rarely compared directly to theory. Ruffato et al. experimentally optimized the layout of interdigitated electrodes and found that it qualitatively matched results from finite element simulations [26]. The same group separately compared the performance of different electroadhesive shapes [26]. Tellez et al. compared the relationship between shear adhesion to dielectric thickness and voltage for their polymer-based electroadhesive [30]. They found that shear adhesion varied linearly to applied voltage, which

is not consistent with the standard electrostatic force equation that states that force scales quadratically with voltage.

One challenge toward modeling polymer-based electroadhesives is that they are often designed with interdigitated electrodes to adhere to non-conductive surfaces. The electric field between the electrodes polarizes the non-conductive surfaces and generates an electric field [45, 46]. While this architecture is more practical in applications, it also makes these surfaces more difficult to model. To simplify the devices in this work, a single electrode with a dielectric was electrically connected to a conductive surface to generate electrostatic force, shown in Fig. 2.1.

In this paper, fully conductive polymer strips are used so that a parallel plate model can help elucidate the relationships between the critical shear force (defined as the force at which the adhesive separates from the substrate) and design parameters like applied voltage, dielectric thickness, and contact area. The adhesive's thickness is studied as well. Though it is not included in the parallel plate model, thickness is relevant for compliant adhesives because it influences the viscoelastic dissipative mechanism in interfacial fracture [47]. In addition, this paper builds on previous work by the authors [29] and uses fabricated electroadhesives with thin polymer dielectrics ($< 2\,\mu m$) resulting in operating voltages below $100\,V$, an order of magnitude lower than demonstrated in previous work. The consequences of using a thin, higher modulus dielectric to lower voltage requirements are also examined. Finally, failure mechanisms for these electroadhesives were studied using high speed video and are discussed relative to the validity of the proposed frictional model.

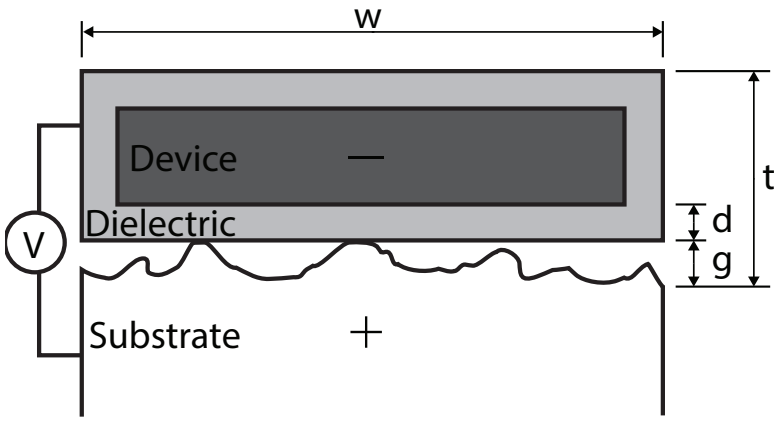

Figure 2.1: Basic operating principal for single electrode electroadhesion. A voltage is applied between a conductive elastomer with a dielectric layer and the substrate.

2.2 Operating Principle

The critical shear force supported between an adhesive and the substrate can be defined by friction or viscoelastic losses from deformations within the adhesive layer, which depend on the shear stresses that the interface can support [48]. The model presented and tested in this paper is a frictional model based on the force normal to the substrate resulting from the applied voltage. In a parallel plate model, electrostatic force exists between oppositely charged plates separated by a dielectric layer and air gap, shown in Fig. 2.1. Air gaps exist because of surface roughness and stiffness in the plates that prevent contact. The electrostatic force between the parallel plates can be described with the following equation,

$$F_{N,EA} = \frac{1}{2}\epsilon_0 V^2 \iint \frac{1}{(g(x,y) + \frac{d}{\sqrt{\epsilon_r}})^2}\, dx\, dy \tag{2.1}$$

where $F_{N,EA}$ is the magnitude of the electrostatic force normal to the substrate, ϵ_0 and ϵ_r are the permittivity of free space and the relative dielectric constant respec-

tively, V is the voltage applied, $g(x, y)$ is the air gap between the dielectric and the substrate at location (x, y), and d is the dielectric thickness.

In a limiting case, it can be assumed that the electroadhesive is compliant and comes in close contact with the surface without any air gaps; the equation can then be simplified as followed,

$$F_{N,EA} = \frac{1}{2}\epsilon_0\epsilon_r A\frac{V^2}{d^2}. \tag{2.2}$$

This equation also assumes that the apparent overlap area A is the true area over which the plates overlap. Each of these assumptions will be examined in greater detail below. In this paper, the critical shear force, the point which the electroadhesive slips, is of interest. It can be defined as the following,

$$F_{S,EA} = F_{N,EA}\mu_f \tag{2.3}$$

where $F_{S,EA}$ is the critical shear force and μ_f is the coefficient of static friction (COF). While μ_f can change with applied normal load for elastomer surfaces [49], this work assumes a constant coefficient of static friction due to the fact that relatively high loads are applied by the electrostatic force. To measure the COF for the electroadhesives in this paper, a sliding friction test was performed on ITO glass four times each for three different electroadhesives at three different normal loads (10 g, 20 g and 50 g). The measured COF over these trials was 2.2 ± 0.6.

Combining Eqn. 2.2 and Eqn. 2.3 suggests that the critical shear force is proportional to the square of the applied electric field. Eqn. 2.4 shows that any

changes to the voltage or dielectric thickness should affect the critical shear force quadratically while area and dielectric constant affect this force linearly. In addition, a smaller dielectric thickness should require a proportionally smaller voltage to achieve the same electric field and supported shear force.

$$F_{S,EA} = \frac{1}{2}\epsilon_0\epsilon_r A\frac{V^2}{d^2}\mu_f \tag{2.4}$$

2.2.1 Air gaps and true contact area

A number of limits to the basic model (Eqn. 2.4) exist in practical use of electroadhesives. Variable gaps can be introduced into the electrostatic model when the electroadhesive does not conform to the substrate. All surfaces have micro and macro roughness and uneven topography that introduce non-uniform air gaps, or surface defects, which reduce the electrostatic force. Debris and particles can create air gaps in the interface, or the adhesive themselves can be warped resulting in larger distances between the surface.

The relative effect of these defects depends on the dielectric thickness and the gaps. The area that encompasses these air gaps have insignificant contribution to the electrostatic force when $g(x,y) >> \frac{d}{\sqrt{\epsilon_r}}$. For example, an electroadhesive with a dielectric thickness of 1 µm and a relative dielectric constant $\epsilon_r = 3.15$ [50] will exhibit a 9 % reduction in force if 10 % of the electroadhesive is separated from the substrate by a 1 µm air gap. At distances past 1 µm the force effectively scales linearly to the fraction of area in direct contact. It is interesting to note that a larger dielectric

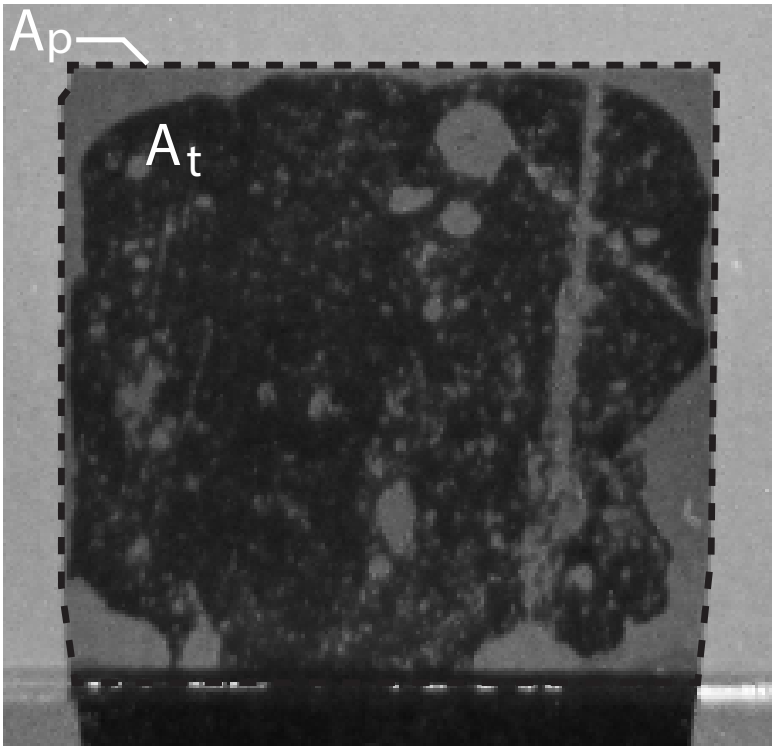

Figure 2.2: View of the interface between the electroadhesive and an ITO-coated glass slide. Portions of the electroadhesive are in close contact (dark gray) while others are separated by air gaps (light gray) due to surface and edge defects. The dark gray areas are defined as the true contact area, A_t. The dashed lines indicate the apparent overlap area, A_p.

thickness implies that the same air gaps will affect the cumulative electrostatic force less than smaller dielectric thicknesses. An electroadhesive with $d = 10\mu m$ would only see a 1 % reduction in force if 10 % of the electroadhesive is separated from the substrate with a 1 µm air gap. However, the tradeoff for a thicker dielectric is that higher voltages are required to achieve similar shear forces as illustrated by Eqn. 2.4.

Another way to consider the effect of variable air gaps and other anomalies on electroadhesives is through apparent and true contact area. The apparent contact area, A_p, is the geometric area of the electroadhesive that overlaps the substrate, but there is no guarantee that this overlap area contributes to overall electrostatic force

due to air gaps. In this work, the true contact area, A_t, is observed through a camera pointed at the interface of the electroadhesive and substrate surface.

An example of contact between an electroadhesive and glass is illustrated in a photograph of the overlap area, Fig. 2.2. Areas separated by large air gaps (light gray) are distributed across the electroadhesive along with areas in close contact (dark gray). The light gray area was considered to not be in close contact (i.e. does not contribute to adhesion), because from experience it was observed that if the surface did not have dark gray areas, then the electroadhesive could not support a measurable shear force. Therefore, the dark gray areas were considered to be the true contact area where adhesion occurs. Unless otherwise noted in the experimental results below, results were gathered for electroadhesives that were visually confirmed with a camera to be in close contact at the start of testing (as close as possible to 100 % dark gray).

2.2.2 Dielectric breakdown

Shear force is also limited by the maximum electric field that can be applied across the dielectric layer. While the first contribution of this work is to characterize electroadhesion in comparison to theory, the second is to demonstrate electroadhesion at lower voltages for simpler integration of electroadhesives for robotics and manufacturing. Parylene C was chosen as a dielectric because conformal deposition of sub-micron layers can be achieved at room temperature. Parylene C has a breakdown field of 220 V/µm [50] which is similar to other common materials used in electroadhesives like Mylar C (245 V/µm with a thickness of 23 µm [51]) and PDMS (250 V/µm at

14 µm thickness [52]). Most of the results in this work were gathered for applied fields below breakdown. However, breakdown can still occur because the dielectric layer thins as the device deforms when shear forces are applied. Experiments in which breakdown occurred were rare and excluded from the results.

Given these practical limitations, the maximum critical shear force that the electroadhesive can sustain is given in Eqn. 2.5 where E_{bd} is the breakdown field and A_t is the true contact area.

$$F_{S,EA,max} = \frac{1}{2}\epsilon_0\epsilon_r A_t E_{bd}^2 \mu_f \tag{2.5}$$

2.3 Experimental setup

2.3.1 Fabrication

As shown in Fig. 2.1, the electroadhesives used in this study are made from a conductive material and a surrounding dielectric. The conductive material used in this work (cPDMS) was prepared by mixing Sylgard 184 polydimethylsiloxane (PDMS) with a carbon black filler (Alfa Aesar, carbon black, acetylene, 50% compressed). To mix the cPDMS, 10 wt% carbon black (relative to PDMS) was stirred with 70 wt% hexane (relative to PDMS) to minimize agglomerations of carbon black. PDMS (10:1 weight ratio of base to curing agent) was then added to the carbon black/hexane mixture and this final mixture was stirred for at least 1 hour using a magnetic stirrer at room temperature.

Before curing the cPDMS on a glass slide, a monolayer of tricholoro(octadecyl)silane

was deposited on the slide. The monolayer of silane was found to be important for a smooth contact surface on the cPDMS and easy release. To deposit a monolayer of silane on glass, the slide was cleaned with acetone, methanol, isopropanol, and DI water. Then it was treated in 100 W O_2 plasma (March Jupiter III O_2 plasma system) to promote adhesion. Finally, it was placed in a vacuum chamber with a few drops of silane and pumped down to 30 kPa and held there for at least 3 h.

The cPDMS mixture was then poured onto the glass slide, squeegeed to a defined thickness, and cured. Due to evaporation of the solvent, the choice of curing temperature and time were critical to fabricate electroadhesives with minimal curling. To make flat electroadhesives that were thicker than 500 µm, the cPDMS was cured in an oven at 60 °C for 16 h. To make electroadhesives thinner than 500 µm the cPDMS was cured at 120 °C for 15 min. These times and temperatures were experimentally determined to minimize curling. Once fully cured, the samples were then cut with a razor blade and coated with parylene C (SCS Parylene Deposition System Model 2010). Dielectric thicknesses were measured by profilometry (Tencor P-20) on a glass slide used as a control during parylene deposition. A small section of each sample was covered with a glass slide during the deposition to later interface with the voltage source.

2.3.2 Test setup

A schematic of the test setup is shown in Fig. 2.3 and an image of the setup used is shown in Fig. 2.4. For each experiment, the electroadhesive was placed on a glass slide

coated with indium tin oxide (ITO) with an overlap area defined by the experiment (nominally 50 mm^2). Before beginning any tests, a PDMS strip was used to lift off debris from the adhesive's surface. A portion of the electroadhesive not in contact with the glass slide was press fit into a polymer clamp along with a 44 AWG wire used to apply voltage to the device. Shear loads were then applied to the sample by moving the polymer clamp with a linear actuator from Thorlabs (PT1-Z8). Shear forces were measured using an ATI Nano17 6-axis F/T transducer.

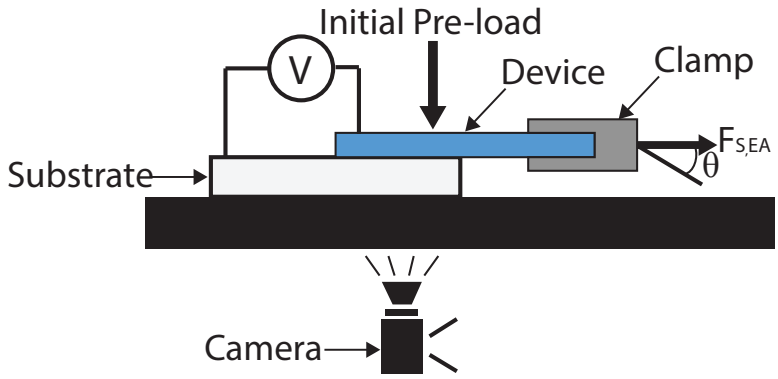

Figure 2.3: Schematic of the experimental setup to measure the critical shear force of an electroadhesive. The substrate is fixed while the electroadhesive is pulled in shear by a linear actuator. A high-speed camera records the changes in contact at the interface during the experiment.

A 50 g weight was used to mechanically pre-load the electroadhesive (corresponding to a normal pressure of approximately 10 kPa). A voltage was then applied between the pad and the ITO-coated glass slide and an image of the interface was used to confirm that the electroadhesive was in contact with the glass slide as illustrated in Fig. 2.2.

Shear loads were applied to the electroadhesive by pulling the clamp at a speed of 0.2 mm/s until either the adhesion failed or the devices broke due to forces exceeding

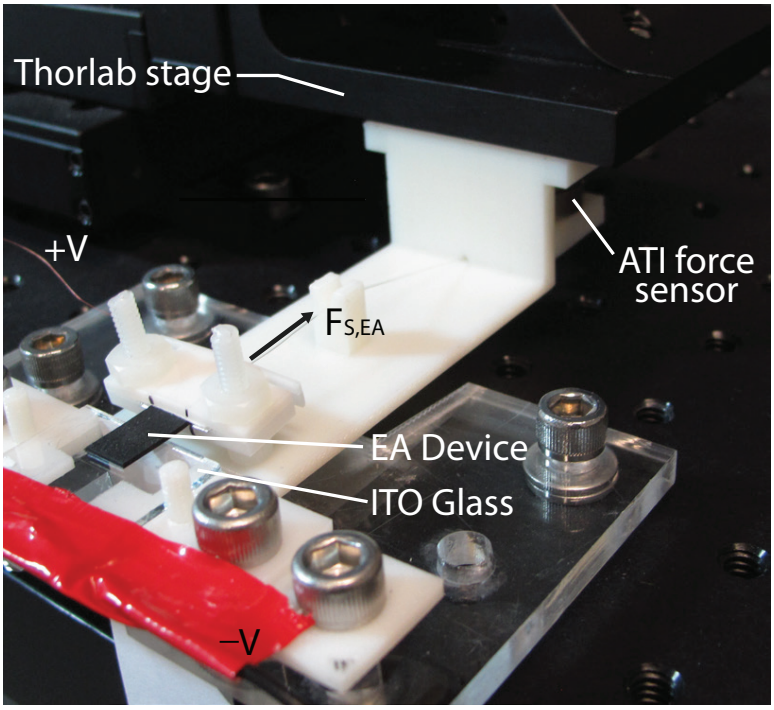

Figure 2.4: A photograph of the experimental setup. The electroadhesive is attached to the force sensor through a clamp and wire. The negative lead is connected to the ITO glass and the positive lead goes to the electroadhesive. A motorized Thorlabs stage is used to pull the electroadhesive in shear at a constant speed of 0.2 mm/s.

their mechanical strength. It was also important that the force applied was parallel to the slide surface. The angle of attack, shown in Fig. 2.3 as θ, was set to zero.

Experimental data showing a typical force versus displacement curve during a shear adhesion experiment is displayed in Fig. 2.5. A high speed camera (Photron Fastcam Mini UX100) was placed beneath the slide and focused on the interface to record contact and failure as depicted in Fig. 2.5. This curve defines the adhesive compliance, similar to that described for bio-inspired dry adhesives [53]. For the electroadhesives in this study, this compliance curve was typically not linear. A higher slope was often seen at the beginning and delamination at the front edge of the electroadhesive led to a lower slope until failure. All failures were sudden and

complete in less than 60 ms.

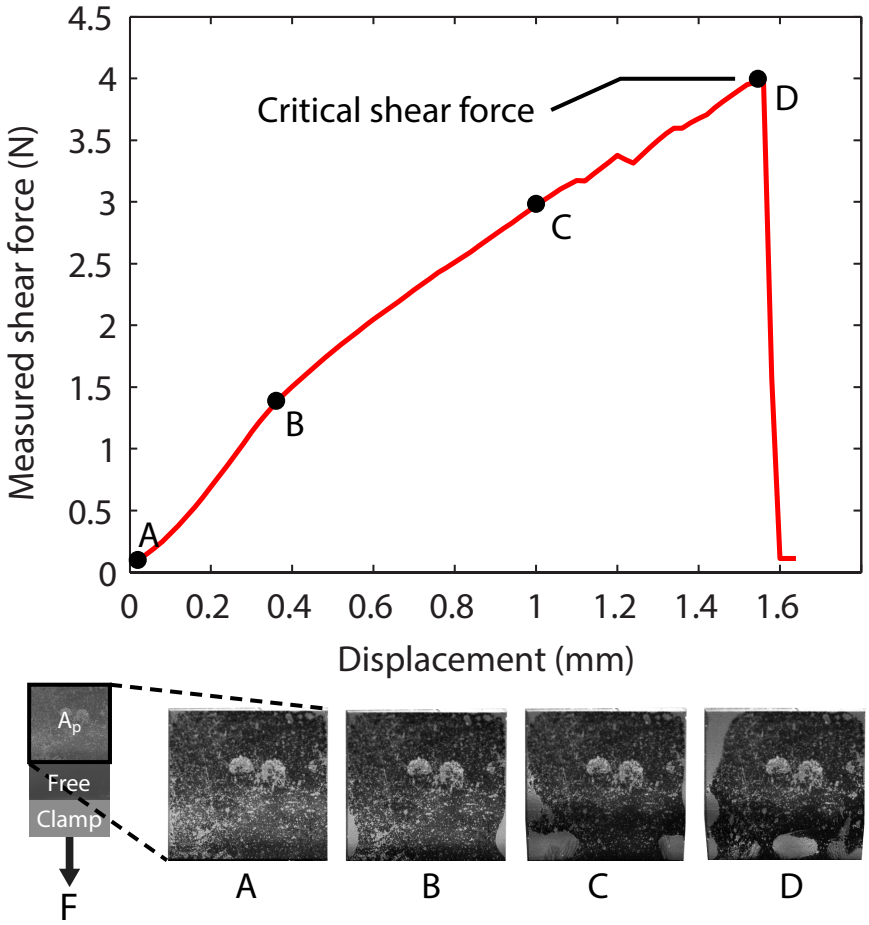

Figure 2.5: Force versus displacement data for a typical shear loading experiment. The force was sampled at 10 Hz with a displacement speed of 0.2 mm/ sec. The bottom insert shows how the true contact area (dark gray) changes at various points during the experiment. A_p shows the section of the device that is nominally in contact with the attachment substrate. The free section is not clamped or over the substrate so it is free to displace, and the clamp section indicates the part of the electroadhesive that is held by the clamp.

2.3.3 Experimental Error

The results below demonstrate that deviations in critical shear force from a single experiment can be quite large; these deviations range from 0.2 N to 2 N. Several factors influenced the performance of electroadhesives: surface defects, curling, and

uneven loading. Surface defects consist of particles and indentations on the adhesive's surface. Dust can be trapped between the dielectric layer and the elastomer during deposition of the dielectric. Indentations are generated from voids within the elastomer when the solvent evaporates. Curling can also create gaps at the edges of the adhesive's interface. Fabricating cPDMS with hexane, a solvent, often caused curling in the device due to internal stress. Curling prevented the edges of the adhesive from fully contacting the surface because in some cases the electrostatic force was not strong enough to counteract the internal stress. Surface defects and curling lowered the true contact area of the adhesive and provided initial cracks for fractures to propagate. Uneven loading caused by slight rotation of the clamp in the plane of the electroadhesive can also lead to deviation in performance. Skewed devices unevenly distributed the shear stress at the fracture front, which led to premature failure.

2.4 Results

To compare the performance of all-polymer electroadhesives with thin dielectrics to the expected value from the frictional theory in Sec. 2.2, three parameters were varied: the dielectric thickness, applied voltage, and contact area. The thickness of the cPDMS was also varied to better understand how geometric parameters affect the critical shear force.

2.4.1 Voltage

As discussed in Sec. 2.2, the critical shear force supported by the electroadhesives should vary quadratically with applied voltage. For this test, the electroadhesive cPDMS thickness was nominally 600 µm, the dielectric thickness was 0.8 µm, and the overlap area was 50 mm^2. Applied voltage was varied in 10 V increments from 10 V to 60 V (corresponding to initial applied fields of 12.5 V/µm to 75 V/µm). Three separate electroadhesives were tested three times each for voltages below 40 V, and four different electroadhesives were tested once for voltages at 40 V and above. The higher supported loads caused wrinkling in the dielectric layer resulting in lower critical shear force upon reuse. Wrinkling will be discussed further in Sec. 2.5.

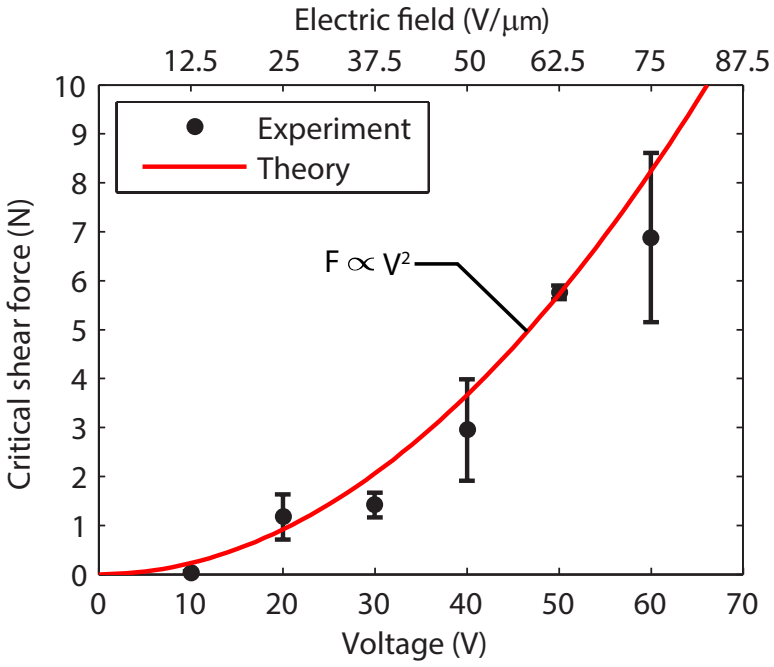

Figure 2.6: Critical shear force measurements versus voltage. Electroadhesives under test had an adhesive thickness and dielectric thickness of 600 µm and 0.8 µm, respectively.

Critical shear force versus applied voltage is shown in Fig. 2.6, and the largest

supported force was 9.2 N (corresponding to 180 kPa) at 60 V. The red 'Theory' line was calculated from Eqn. 2.4 with $A = 50\,\text{mm}^2$, $d = 0.8\,\mu\text{m}$, $\epsilon_r = 3.15$, and $\mu_f = 2.2$. Although there was variability in the results, it is clear that the critical force increases quadratically with voltage as predicted. It was visually observed in these tests that at voltages below 40 V the true contact area varied between 50 % to 70 % of the apparent area. At 10 V for example, no contact was observed for some samples, yielding no measurable adhesion. The variation in contact area can be attributed to surface defects and the bending rigidity of the adhesives. At low voltages, the electrostatic force could not overcome those factors which resulted in reduced contact.

2.4.2 Dielectric thickness

Critical shear force should also vary quadratically with the dielectric thickness according to Eqn. 2.4. To study this scaling, electroadhesives with a cPDMS thickness of 600 µm were tested with an applied voltage of 40 V. Dielectric thicknesses studied ranged from 0.38 µm to 1.4 µm resulting in applied fields varying from 105 V/µm to 29 V/µm, still well below breakdown for parylene. At least four electroadhesives were tested once for each dielectric thickness.

For dielectric thickness greater than 0.7 µm, decreasing the thickness was shown to increase shear forces quadratically as expected. However, dielectric thicknesses below 0.7 µm did not follow theoretical predictions; the electroadhesives underperformed. One hypothesis is that the adhesives are prematurely failing because of a lower effective modulus. An effective modulus for the tensile load can be calculated as

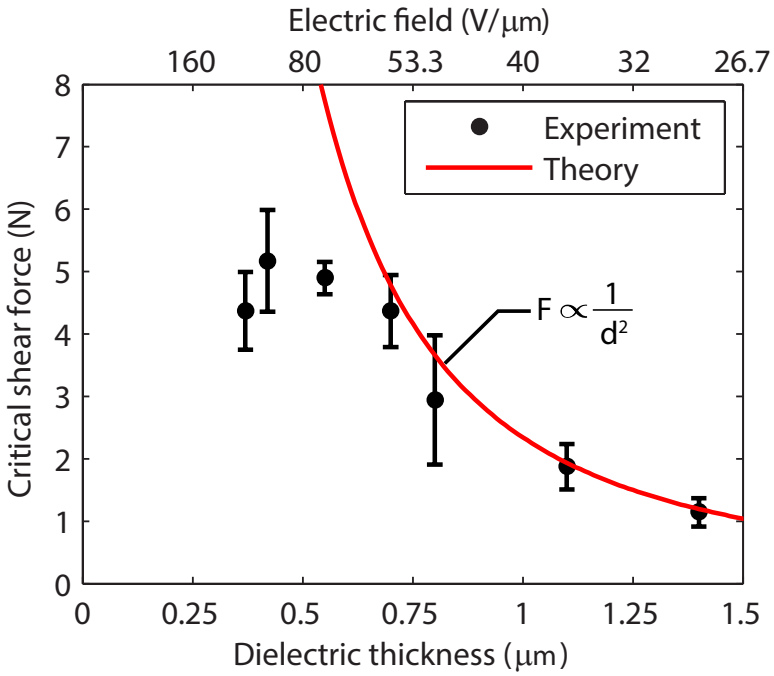

Figure 2.7: Critical shear force as a function of dielectric thickness. These electroadhesives had an adhesive thickness of 600 µm and were tested at 40 V.

$E_{eff} = (2E_p t_p + E_c t_c)/(2t_p + t_c)$ where E_p is the modulus of parylene (2.8 GPa) [50], E_c is the modulus of the cPDMS electrode (approximately 1 MPa) [54], t_p is the parylene thickness, and t_c is the cPDMS thickness (600 µm). This effective modulus varies from 4.5 MPa for the thinnest dielectric devices to 14 MPa for the thickest dielectrics. Compared to higher modulus devices, lower modulus adhesives require larger strain to obtain similar shear forces. This increases the Poisson's effect, which contributes to multi-direction shear forces at the delamination front, resulting in faster failure.

2.4.3 Area

The critical shear force should vary linearly with contact area, Eqn. 2.4. Experiments were run using electroadhesives with an average adhesive thickness of 650 µm,

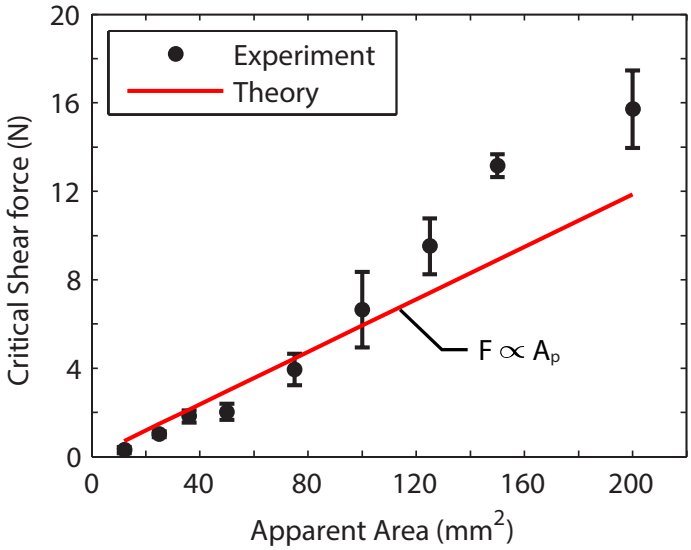

Figure 2.8: Dependency of adhesion force on apparent contact area. The voltage applied was large enough such that the true contact area was approximately equal to the apparent contact area. These electroadhesives were tested at 40 V with an adhesive thickness and dielectric thickness of 650 µm and 0.9 µm, respectively.

a dielectric thickness of 0.9 µm and an applied voltage of 40 V. A square contact area was maintained for each experiment with contact areas ranging from 12.25 mm^2 to 200 mm^2. For each experiment it was visually confirmed that the adhesives were as close as possible to full contact with the surface at the start of the experiment. It was observed that the average true contact was (90 ± 4) % of the apparent area. Some devices did not yield full contact because of warped edges or surface defects. Five devices were tested once for each area.

It is shown in Fig. 2.8 that below 125 mm^2 adhesion varies linearly to apparent contact area. The trend, however, begins to deviate beyond 100 mm^2, yielding critical shear forces that are significantly larger than predicted. Higher critical forces are likely enabled by a larger ratio of adhesive lateral dimension to thickness that can reduce the likelihood of edge crack propagation as a method for failure [35]. This will be

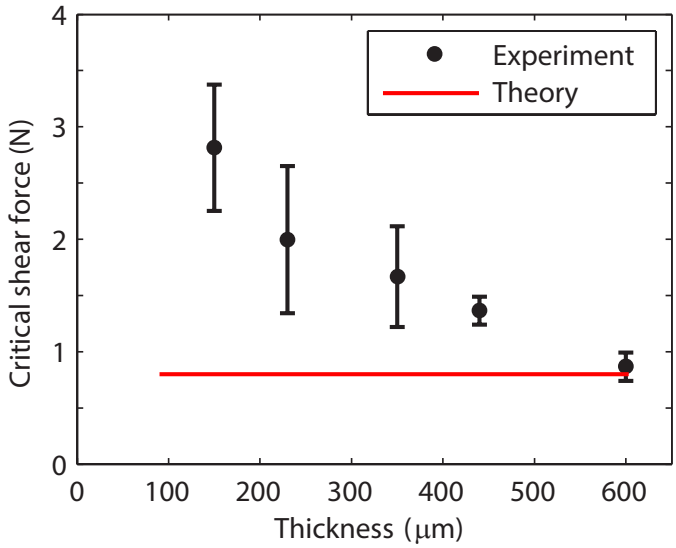

Figure 2.9: Critical shear force measurements versus cPDMS thickness. Electroadhesives were tested at 25 V and had a dielectric thickness of 1.1 µm.

discussed further in Sec. 2.5.

2.4.4 Adhesive Thickness

Previous work on compliant adhesives has demonstrated that the critical shear force varies with material and geometric properties, including parameters like thickness and width. The thickness of the adhesive (or adhesive backing) can play a large role in critical force, though it is not accounted for in Eqn. 2.4 [47, 55–58]. To better explore this relationship, electroadhesives were fabricated with five different cPDMS thicknesses ranging from 150 µm to 600 µm. The dielectric layer for all of the electroadhesives was 1.1 µm and the overlap area was kept constant at 50 mm^2. For each thickness, at least four devices were tested once at 25 V. The tests were conducted at 25 V because at higher voltages the thinner adhesives supported shear loads that exceed their ultimate tensile strength.

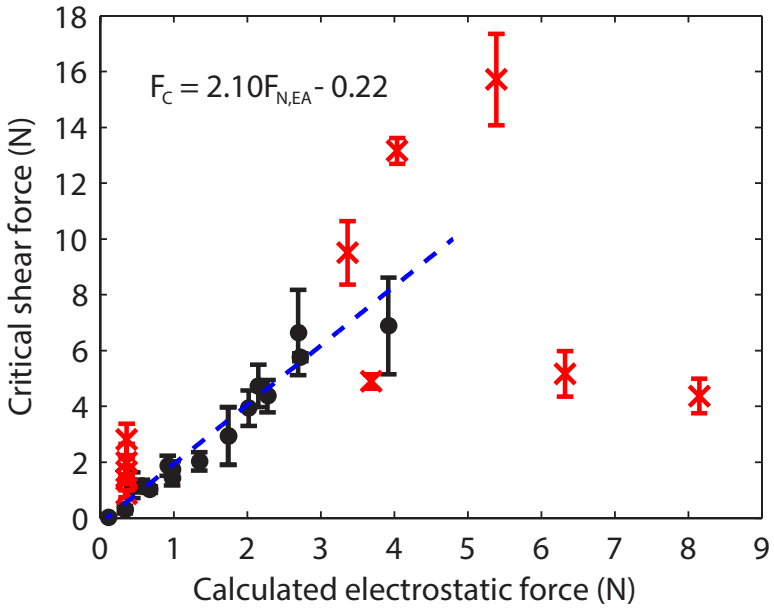

Figure 2.10: Critical shear force measurements for all samples versus expected electrostatic force from the model in Eqn. 2.2. The dashed line represents a weighted fit to the data that matched the model (black dots). Data marked in red represent deviations from the model as identified in previous sections.

Fig. 2.9 demonstrates that thinner devices supported far larger critical shear forces. The thinnest adhesives (150 µm) supported shear forces up to 3.3 N, which was 3 times greater than the forces obtained by the thickest adhesives (600 µm), 1 N. Similar to the large area adhesives, higher critical forces are likely enabled by a larger ratio of adhesive lateral dimension to thickness. This is discussed further in Sec. 2.5.

2.5 Discussion

2.5.1 Basic friction model validity

The results indicate that electroadhesives fabricated using a single cPDMS electrode and parylene dielectric match the basic friction model in Eqn. 2.4 for samples tested with dielectric thicknesses $d > 0.7\,\mu m$, area $A < 125\,mm$, and cPDMS thickness $t \simeq$

600 µm. A weighted fit to this data shown in Fig. 2.10 results in a coefficient of friction of approximately 2.1 which matches the measured coefficient of friction, 2.2 ± 0.6.

Deviations from this model as described in Sec. 2.4 are indicated by red x's in Fig. 2.10. Red x's above the dashed line performed better than predicted by the friction model. We hypothesize that this improved performance is due in part to the geometry of the adhesive, specifically the ratio w/h where w is the adhesive length and h is the adhesive thickness. Crosby et al. proposed that the geometric confinement defined by this ratio would lead to different failure mechanisms [35]. Fig. 2.11 plots the inverse of the effective modulus multiplied by the adhesive length $1/(E_{eff} * w)$ versus the w/h ratio, where h is taken as the cPDMS thickness. The black dots are the devices that follow the friction model in Fig. 2.10 and the red x's represent the devices that deviated. There is a clear clustering of results in this plot and electroadhesives that performed better than predicted by the model are shown far out along the w/h axis.

Electroadhesive indicated by red x's below the dashed line in Fig. 2.10 failed before expected by the model. They are also represented in the red x's above the black dots in Fig. 2.11. These cases were defined by dielectric thicknesses < 0.7 µm. The lower effective modulus in these devices result in larger displacements applied by the test setup for the same shear force. These higher strains result in significant deformation in the electroadhesive at the edge of the glass slide as shown in Fig. 2.12(C). The contraction of the electroadhesive due to Poisson's ratio provides additional stresses at the interface leading to failure.

It should also be noted that these high strains also ultimately lead to failure in

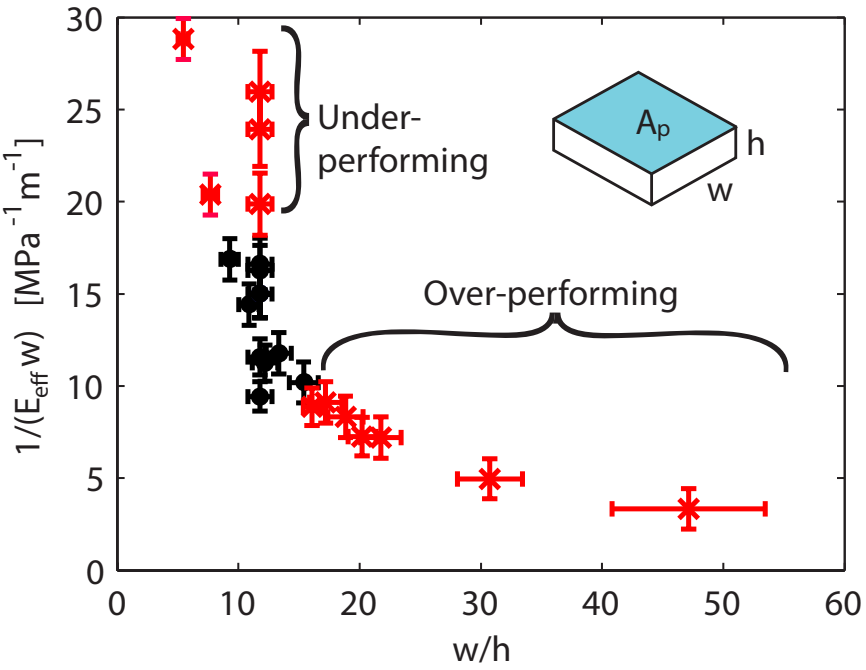

Figure 2.11: Clustering of experimental results based on geometry and effective material modulus of the cPDMS/parylene composite. The error bars represent the uncertainty in the measurement of the parylene and cPDMS thickness, 0.02 µm and 25 µm, respectively.

all electroadhesives that deviate from the basic friction model (Fig. 2.12(A/C/E)). This figure compares the electroadhesive interface in its initial state, under load, and just prior to failure. These images from the captured high speed video were used to determine how true contact area changed as higher shear loads were applied to the electroadhesive. Columns A and B are electroadhesives with a 200 µm and 600 µm cPDMS layer respectively. The 600 µm thick device shows obvious edge crack propagation at failure while the 200 µm thick device in column B shows significant deformation due to large applied strain and a different failure mechanism. This electroadhesive example exhibited healing cracks and detachment waves, similar to Schallamach waves [59,60] indicated by the red arrows. Columns D and E show failure in a 75 mm and 200 mm electroadhesive respectively. Electroadhesives with smaller

apparent contact areas that matched the model showed the edge crack propagation while the larger area devices showed detachment waves. The waves, a form of sliding friction phenomenon seen in carbon-filled rubbers, were observed at high strains and have been attributed to increasing shear loads [60, 61]. Sliding friction is a form of viscoelastic dissipative mechanism that reduces the energy to propagate the crack front. This allows the interface to sustain larger shear loads [48, 62]. Sliding friction was also seen in the thin dielectric example $d = 0.42\,\mu\text{m}$ in Column C because it experienced high strains.

2.5.2 Repeatability

One drawback to decreasing the dielectric thickness and use of parylene as a dielectric material is reduced mechanical robustness. Thinner layers are more susceptible to wrinkling and small particles penetrating the surface. Wrinkling occurred because of a large differential in strain deformation between the parylene and cPDMS layer, the former plastically deforms and the latter elastically deforms. Parylene has a tensile modulus of 2.8 GPa and a yield strength of 55 MPa. cPDMS has a tensile modulus of 1 MPa. After 2 % strain, parylene will begin to plastically deform [50]; cPDMS can return to its relaxed state without significant permanent deformation for strains up to 80 % strain. Electroadhesives typically experience strains above 20 % strain before failure. When the applied stress is relaxed, the cPDMS will relax to its original state causing the thin parylene layer to compress and wrinkle on the surface. This wrinkling is shown in Fig. 2.13. The wrinkled parylene layer increases

roughness on the cPDMS surface, preventing close contact upon reuse, which can result in decreased performance. If large sections of the contact area are wrinkled, subsequent shear adhesion suffers due to lower contact.

Replacing the dielectric with a more compliant material, such as PDMS, could improve robustness in the future. As mentioned earlier, at 14 µm thick PDMS has a breakdown voltage of 250 V/µm, which is similar to parylene C. However, using PDMS would increase the voltage requirement because it is difficult to achieve sub-micron thick layers. Lower thicknesses can be obtained with PDMS [63]; however, there may be pinholes. In addition, use of PDMS will also result in large adhesive forces when no voltage is applied. If a large adhesion differential is desired, other materials might be preferred.

Future electroadhesives may also take advantage of the work in Bartlett et al. that used fabrics to prevent significant extension or contraction in the adhesive plane while maintaining compliance in the direction normal to the adhesive interface [16]. This approach could also solve the problem of large stresses orthogonal to the direction of shear force due to Poisson's effect.

2.5.3 Application

In this work, adhesion is achieved by applying a voltage between a single cPDMS electrode and a conductive surface. This simple setup is limited to applications where the surface is conductive and can be tethered to the voltage source. However, the results from this paper show that electroadhesion can be a versatile mechanism that allow

users to easily tailor the maximum critical shear force the adhesive can achieve by adjusting design parameters such as dielectric thickness, contact area, and adhesive thickness. Use of variable applied electrostatic force also provides users the option to actively tune adhesion over large ranges by adjusting the voltage. A device with a contact area of 50 mm^2 and dielectric thickness of 1 µm, can theoretically obtain critical shear forces from 0 N to 75 N (or 0 kPa to 1500 kPa) for voltages between 0 V and 220 V, given Parylene's dielectric strength of 220 V/µm. While gecko adhesives do not require any external power to operate, they cannot easily change adhesion strength. Tunable adhesives can be advantageous in applications such as climbing, turning for small legged robots or pick and place in manufacturing [20, 22, 23, 64].

It is important to note that dielectric thicknesses used in this paper are small relative to previous work [4, 26, 30]. Most electroadhesives require kiloVolts to obtain similar shear pressures shown in this paper because their dielectrics are tens of microns thick. Sub-micron dielectrics can be used to reduce electrical components for high voltage converters by lowering the voltage requirement for adhesion. However, in the electroadhesives designed for this work, the benefits of sub-micron dielectric diminish as the thickness decreases past 0.7 µm. Below 0.7 µm the increase in adhesion was marginal and thinner dielectrics reduced the robustness and repeatability of electroadhesives.

While this model was able to predict the critical shear force for an electroadhesive device, it was limited to a small range of design parameters. Furthermore it was demonstrated that compliance affects adhesion however the basic friction model does not predict or explain why compliance affects adhesion. To develop a more

general model to predict the effect of electrostatic force in soft electroadhesives while accounting for compliance, a different approach will be taken in the next chapters.

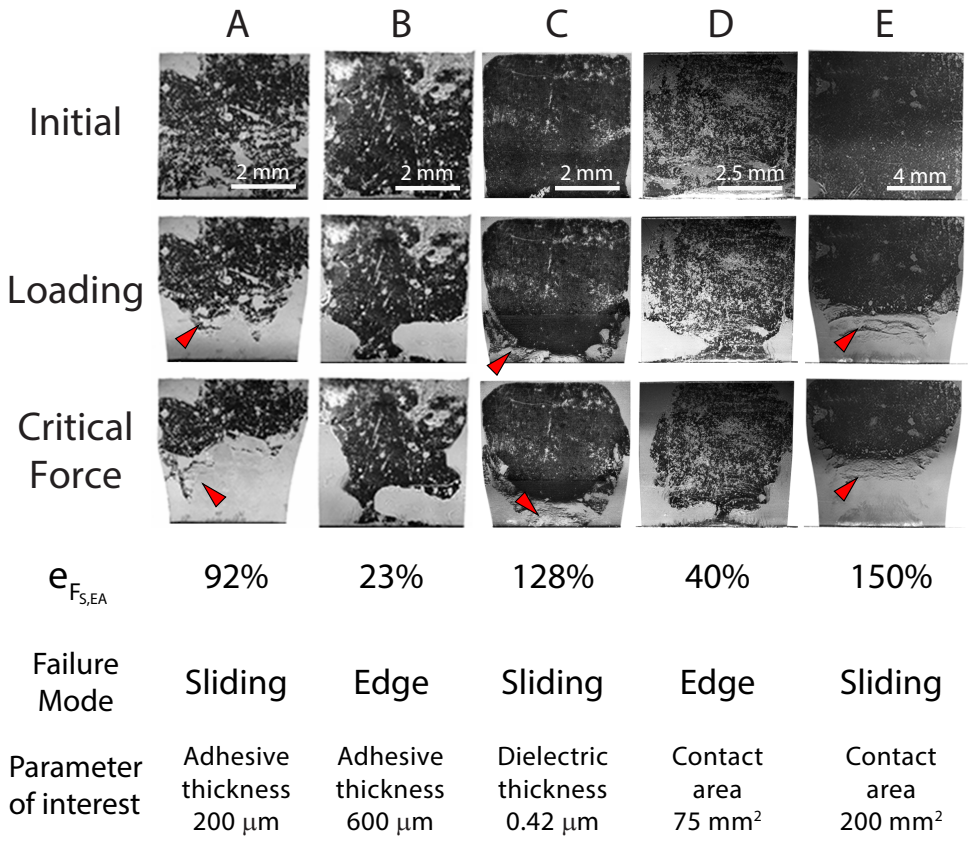

Figure 2.12: Comparison of true contact area during testing for devices with different adhesive thickness, dielectric thickness, and apparent contact area. The row labeled $e_{F_{S,EA}}$ is the engineering strain at the critical shear force. (A-B) are devices with adhesive thicknesses of 200 µm and 600 µm, respectively. C) has a thin dielectric of 0.42 µm. (D-E) have apparent contact areas of 75 mm^2 and 200 mm^2, respectively. The images for (D-E) have been digitally scaled down to have the same dimensions as (A-C). The first row is the initial state of the device's contact area (dark areas) before loading. The second row is the image of the device under load, and the third row is the image of the contact area at the critical shear force. The red arrows indicate areas where interfacial sliding was observed.

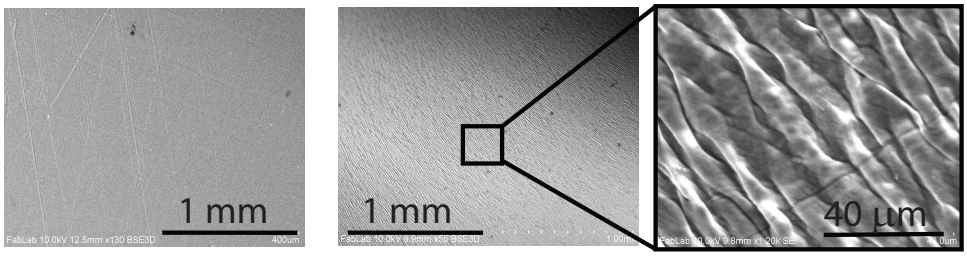

Figure 2.13: A) SEM image of a sample with no wrinkling. B) A SEM image of a sample with significant wrinkling after being plastically deformed. C) Close-up of the wrinkling. Image credit: Aaron Gerratt.

Chapter 3

Modeling Electrostatic Force with Energy Release Rate

Controllable adhesives have material properties that allow them to easily bond and debond to surfaces with an external stimulus. They have been developed for disassembly and repair of bonded components, painless removal of medical tapes on wounds, and sutureless adhesive films in surgery. [65–68]

There are many types of controllable adhesives, some use temperature to break the polymer structures for debonding, others use polymers that react to pH or UV light to bond and debond [66–68]. Another method to control adhesion is electroadhesion (EA) in which electrostatic force is used to increase adhesion of soft conductive polymers. Electroadhesives have been demonstrated for adhesion on multiple types of substrates, gripping in soft actuators, and turning in small legged robots. [1, 4, 20, 27]

The basic principle of electroadhesion relies on using an applied electric field to generate electrostatic force between the adhesive and the surface. The increased normal load also increases the holding force of the adhesive. The strength of the electrostatic force depends on contact area, applied electric field, and polarizability of the attachment surface [26, 30, 44]. Soft EAs are typically made of elastomers so the behavior of their adhesion without an applied voltage can be described by Johnson-Kendall-Roberts (JKR) theory, which relates the material property and compliance of the polymer to adhesion. [36, 38, 39] Therefore, it is important to understand the con-

tribution of both electrostatic force and the polymer's material properties to adhesion and delamination of soft EAs.

The effects of compliance, material properties of the polymer, and chemical bonds at the interface have been well characterized using JKR theory, however, little work has been done to examine the added effect of introducing electrostatic force. Hays looked at how charged plastic particles adhere to surfaces due to electrostatics and van der Waals [69]. However, they had difficulty parsing out the effect of electrostatics in adhesion of their particles, in part, because of contact electrification, where the surface charge of the particles change after contact with the surface. Tian modeled electrostatic force on a particle as a Hertzian load and incorporated it into the JKR equation. [70] They modeled the electrostatic force using the method of image charges, where particles of radii around 100 µm were treated as point charges with the force acting at the center of the particle. This can be used for spheres with sufficiently small radii and contact radii, however for this paper we are interested in contact with spheres that are orders of magnitude larger and with finite contact areas where the method of image charge is not valid. [71]

Here, we set out to develop an analytical model for soft electroadhesives by investigating the combined effect of electrostatic force and polymer adhesion in conductive elastomers. We first describe electrostatic force in terms of critical energy release rate to more easily incorporate this effect into JKR theory. Then we investigate the contribution of electrostatics to adhesion in conductive elastomers. Sec. 4.1 will lay out how electrostatic force is introduced into the JKR framework and its consequence. Sec. 3.2 describes the experimental setup for the electrostatic tack tests

and Sec. 3.3 analyzes the results of the tack tests and includes a discussion of their implications.

3.1 Theory

3.1.1 Rigid sphere, elastic half-space

Critical energy release rate (G_c) is a measure of the driving force required to break the bonds (chemical or mechanical) responsible for interfacial adhesion. Linear fracture analysis can be used to calculate the driving force for fracture for a rigid sphere in contact with an elastic half-space; assuming a linear elastic response, the driving force for crack propagation is given by

$$G = \frac{(P' - P)^2}{4\pi R}\frac{dC}{da} \tag{3.1}$$

where G is the energy release rate, P' the Hertzian load, P the measured load, a the contact radius, R the radius of the sphere, and C the compliance of the elastic half-space, shown in Fig. 3.1A. [36] Assuming there is no friction at the interface (i.e. no lateral stresses at the edge of contact) the compliance of the elastic half-space becomes [36]

$$C_0 = \frac{1}{2E^* a} \tag{3.2}$$

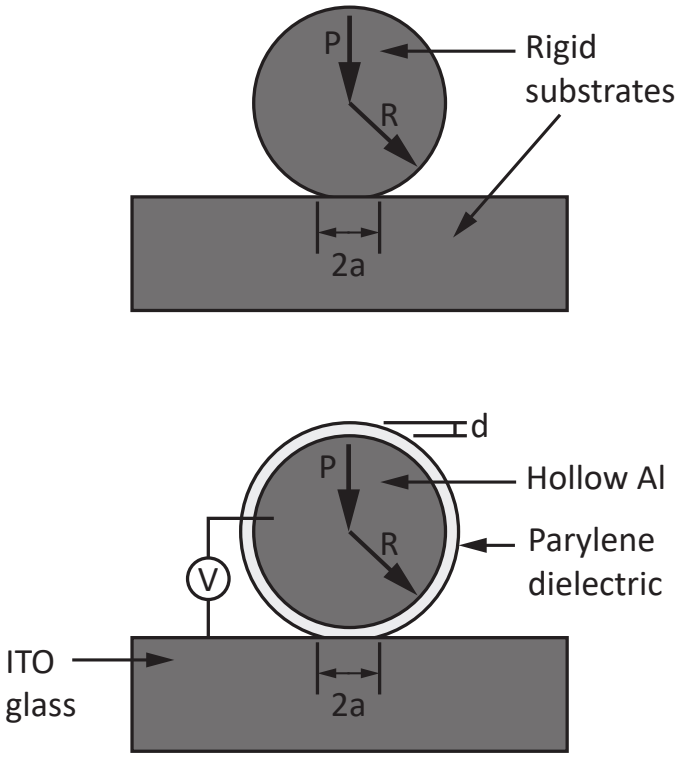

Figure 3.1: A) Schematic of a tack system where a rigid sphere contacts a elastic half-space. R is the radius of the sphere, P is the measured load on the probe, and a is the contact radius. B) Schematic of the tack system for a rigid probe contacting an elastic half-space, with the added option to apply a voltage. The rigid probe is a hollow aluminum sphere with a radius, R, of 6.35 mm and a dielectric coating, d, 1.5 µm thick. A voltage, V, can be applied between the conductive probe and ITO glass.

where E^* is the effective modulus of the half-space which is related to Young's modulus, E, through

$$E^* = \frac{E}{(1-\nu^2)} \tag{3.3}$$

and ν is the Poisson's ratio which is assumed to be 0.5 for the elastomers used in this paper. By combining Eqn. 3.1 and Eqn. 3.2 for the case where the contact radius is significantly smaller than the probe radius ($a/R \to 0$), energy release rate can be

expressed as

$$G = \frac{(4E^* a^3/R - P)^2}{8\pi E^* a^3} \tag{3.4}$$

The critical energy release rate at fracture can be described as

$$G_c = \frac{2P_C}{3\pi R} \tag{3.5}$$

where P_c is the load at which adhesive failure occurs [36].

The electrostatic force between a conductive plane and sphere is typically derived using the method of image charges. The sphere is reduced to a point charge with a force acting at the center and the conductive plane is replaced with an image charge with the same but opposite charge as the original sphere. This is valid for when the sphere is sufficiently far away from the plane and small enough such that it can be treated as a point charge without any consideration of geometry. Tian used this method to describe the electrostatic force on the adhesion of small plastic particles to surfaces [70]. This assumption is not valid in our system because the spherical indenters that were used are orders of magnitude larger than the distance it is away from the conductive plane, in which case, geometry and contact area cannot be ignored. Crowley derived the electrostatic force for a conductive sphere and plane, at close contact ($d/R \to 0$), shown in Fig. 3.1B. [71] The change in electric field due to the geometry of the sphere was taken into account, and the force can be approximated by the following equation

$$P_v = \frac{\epsilon \pi V^2}{\zeta + \zeta^2} \tag{3.6}$$

where $\epsilon = \epsilon_0 \epsilon_r$ and ϵ_0 and ϵ_r are the permittivity of free space and the dielectric constant of the insulating layer, respectively, V is the applied voltage between the conducting sphere and plane, and $\zeta = d/R$, where R is the radius of the sphere and d is the distance between the sphere and plane, and in the case of contact, the dielectric thickness. Eqn. 3.6 can be further simplified for when $R >> d$, since ζ^2 approaches zero, such that the equation can be simplified to

$$P_v = \frac{\epsilon \pi R V^2}{d} \tag{3.7}$$

In a tack system where both the indenter and elastic surface are made of rigid materials, adhesion forces due to surface energy and van der Waals are extremely low, and in our system, adhesion could not be detected at the force ranges of mNs. An applied electrostatic force in this system dwarfed any adhesive force from surface energy or van der Waals, so the tack force, when voltage was turned on, was assumed to be solely due to electrostatics. And in a traction free system this tack force can be predicted by the electrostatic force given by Eqn. 3.7, such that $P_c = P_v$.

The adhesive force due to electrostatics can then be described in terms of critical energy release rate by combining Eqn. 3.5 and Eqn. 3.7, giving the following expression,

$$G_v = \frac{2\epsilon V^2}{3d} \tag{3.8}$$

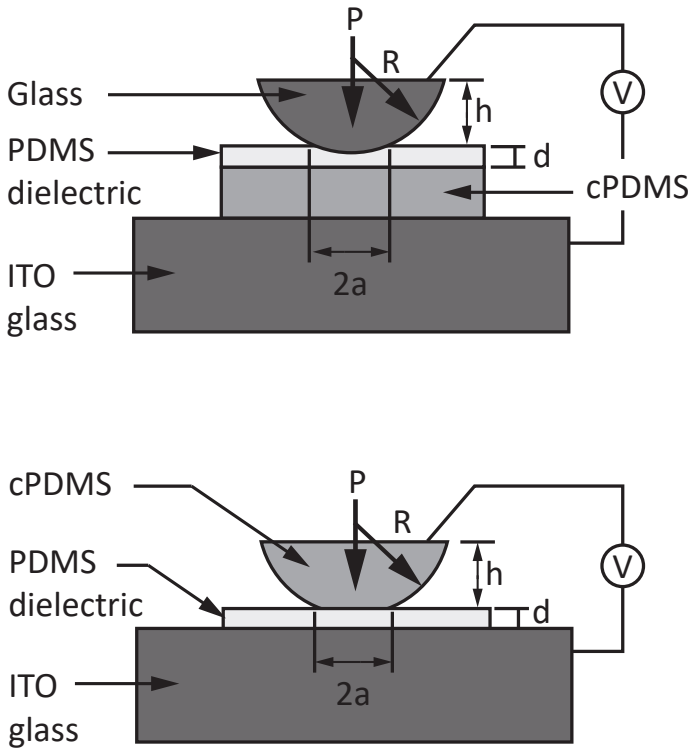

Figure 3.2: A) Schematic of the tack system where a rigid sphere contacts a compliant layer made of cPDMS with a thin PDMS acting as the dielectric layer. The glass probes with radii of 3, 4 and 5 mm were used to contact cPDMS layers with thicknesses of 0.8 mm and 2.1 mm. The dielectric layer was 7 µm thick and a voltage was applied to the glass probe and ITO glass slide. There was no need to apply the voltage directly to the cPDMS layer because the cPDMS was electrically connected to the ITO slide through contact. B) Schematic of the second tack system to test the superposition theory, Eqn. 4.1. A compliant probe made of cPDMS with a radius of 4 mm was brought into contact with an ITO glass slide with a 7 µm thick PDMS dielectric. The height of the probe was 4 mm.

showing that G_v scales with applied voltage squared and the inverse dielectric thickness.

3.1.2 Rigid sphere, compliant layer

To introduce polymer adhesion into the system, a compliant layer with a finite thickness replaced the rigid elastic half-space, the schematic is shown in Fig. 3.2A. With a rigid indenter contacting soft elastomer layer, adhesion at the interface due to van der Waals forces and viscoelastic dissipation can be measured. It was assumed that viscoelastic dissipation occurred only near the crack tip and that there were no bulk viscoelastic effects. When contacting compliant layers, finite size effects will change the compliance of the system based on the ratio of the contact radius to the thickness of the polymer layer (a/h) [37]. In addition, contact between the probe and polymer layer will have lateral stresses at the interface, so including a full friction boundary condition is a closer approximation to the real system. By taking into account finite size effects, the compliance of the polymer layer can be approximated by the following expression:

$$C = \frac{1-\nu^2}{2Ea}\left(1+\left(\frac{0.75}{a/h+(a/h)^3}+\frac{2.8(1-2\nu^2)}{a/h}\right)^{-1}\right)^{-1} \tag{3.9}$$

Combining Eqn. 3.1 and Eqn. 3.9 and assuming $\nu = 0.5$, the driving force for fracture can be calculated for every point during the JKR tack test with the following equation

$$G = \frac{0.022(P'-P)^2}{Ea^3}\left[\frac{0.75+2(a/h)+4(a/h)^3}{(0.75+a/h+(a/h)^3)^2}\right] \tag{3.10}$$

where P' is the modified Hertzian load with a full friction boundary condition,

$$P' = \frac{16Ea^3}{9R}(1 + 0.33(a/h)^3) \tag{3.11}$$

When the crack actually propagates through the interface, energy is expended by creating new surfaces and through viscoelastic loss near the crack tip. The lower limit of G during an advancing crack is set by the thermodynamic work of adhesion, $w = \gamma_A + \gamma_B - \gamma_{AB}$. The surface energy of the probe and surface is γ_A and γ_B, respectively, and γ_{AB} is the free energy of the AB interface. At very low crack velocities, where viscoelastic dissipation can be ignored, G approaches w. However, at crack velocities where viscoelastic losses at the crack tip will contribute to the driving force for fracture, the energy to propagate crack growth can increase significantly. These viscoelastic losses are dependent on the crack velocity, v, where $v = -da/dt$. The rate of crack propagation is determined by a material dependence of G and v, which can be expressed by the following empirical relationship,

$$G = G_c\left(1 + \left(\frac{v}{v^*}\right)^n\right) \tag{3.12}$$

where v^* is the characteristic crack speed and n is a material dependent parameter.

For receding cracks (i.e. increasing contact radius) the upper limit of G is the thermodynamic work of adhesion. Viscoelastic dissipation also contributes to the energy release rate of a receding crack, G_a, such that it can be expressed as [38]

$$G_a = w(1 + \Phi(a, v)) \tag{3.13}$$

Where $\Phi(a, v)$ is the viscoelastic dissipation which is dependent on the contact radius, a, and crack velocity, v.

Electrostatic force operates at a different length scale compared to van der Waals or chemical bonds that make polymers adhere to surfaces. Therefore, it is assumed that electrostatic force is independent of the mechanisms that govern the adhesive property of the polymer. Consequently, the driving force for fracture of the polymer, $G_c|_{0V} = G_o$ at zero voltage, is unaffected by electrostatics; furthermore, in a tack system with electrostatic force, the critical energy release rate of the system is hypothesized to be a superposition of the polymer's and electrostatic's critical energy release rate, such that

$$G_c = G_0 + G_v \tag{3.14}$$

where G_c, G_o, and G_v are the critical energy release rate of the system, polymer, and electrostatic force, respectively. Combining Eqn. 4.1 and Eqn. 3.7 together, reveals how an applied voltage is hypothesized to affect G_c

$$G_c = G_0 + \frac{2\epsilon V^2}{3d} \tag{3.15}$$

3.2 Experimental Setup

Standard JKR tack tests were conducted with spherical indenters made of different materials: hollow aluminum balls, glass hemispheres, and conductive elastomers hemispheres. For all the probes, the tack test procedures were the same. The indenters were attached to the end of a laser-cut acrylic cantilever beam that was mounted to a 6-axis ATI nano17 force sensor, shown in Fig. 3.3. The tack force experienced by the probe was measured as a moment by the force sensor. For all experiments, the linear stage PT1-Z8 from Thorlabs was used to bring the probe into contact with the surface (i.e. ITO glass slide from Sigma Aldrich or a conductive polymer layer) at a speed of 6.0 µm/s. A 10 mN mechanical preload was reached before unloading at 6.0 µm/s. Due to unreliable readings from the linear stage, the displacement of the probe was not measured. There was an approximate 2 s wait time between loading and unloading the probe, this was due to backlash in the linear stage. To apply electrostatic force, a voltage was applied between the probe and the contacting surface using a Keithley 2410 sourcemeter before loading and kept on until unloading was complete.

3.2.1 Rigid sphere, elastic half-space

To verify Eqn. 3.7 and describe electrostatic force in terms of critical energy release rate, two rigid materials were used so the only measureable adhesive force was from electrostatics, Fig. 3.1B. Hollow aluminum balls with a radius of 6.35 mm from McMaster-Carr were used as the rigid indenters and a 2 mm thick ITO glass slide

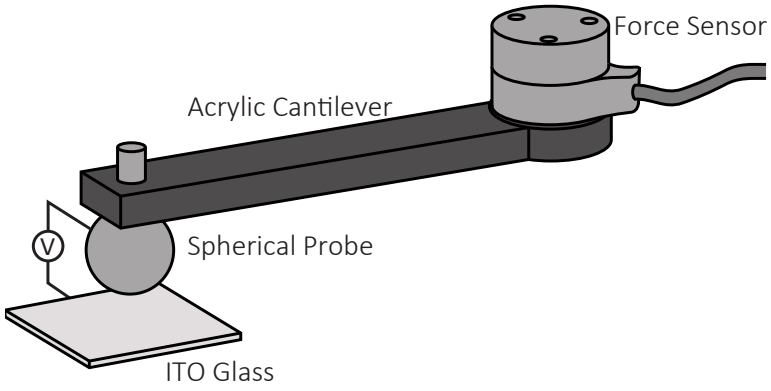

Figure 3.3: Schematic of the experimental setup. A conductive probe, in this example, a sphere, is attached to the end of a cantilever beam. The beam is attached to a 6-axis force sensor that measures the torque exerted on the beam. The force sensor is connected to a linear motor (not shown) that moves the sensor and cantilever beam vertically to bring the probe in and out of contact with the ITO glass.

from Sigma Aldrich was the elastic half-space.

Parylene C, a dielectric, was used to insulate the indenter when contacting the ITO slide. Parylene C was selected since it did not exhibit any measureable adhesion when in contact with glass. It also has a tensile modulus of 69 MPa which is significantly stiffer than any typical elastomer, therefore, deformation of the layer was ignored in the measurements [50]. To promote adhesion of the dielectric layer to the metal balls, the metal balls were submerged in a 100:100:3 volume ratio of DI water, IPA, and A-174 silane from Sigma Aldrich for 30 min, before coating with Parylene. Afterwards, the spheres were air dried using N_2 gas and placed inside of a SMS Parylene coater and coated with a layer of dielectric. A dielectric thickness of 1.5 µm was measured on a test glass slide that was placed in the chamber with the probes. There was an uncertainty of approximately 0.1 µm in dielectric thickness due to the deposition process. This was based on profilometry measurements at various points on the test glass slide using a P-20 profilometer from Tencor.

The finished probes were then attached to the cantilever beam and adhesion was measured by pressing the aluminum probe into the ITO glass slide. At least three trials were taken for voltages ranging from 0 V to 140 V at 20 V increments. This was done with two separate probes fabricated in the manner described.

3.2.2 Rigid sphere, compliant layer

Eqn. 4.1 was tested by conducting JKR tack tests on two different adhesive systems, one with a rigid probe contacting a soft polymer layer and the other a compliant probe contacting an elastic half-space. For the first system, a rigid probe contacting a compliant layer was used to measure the combined effect of electrostatic and polymer adhesion, shown in Fig. 3.2A. Glass half-ball lenses from Edmund optics were used as indenters to contact a layer of conductive polymer. Glass hemispheres were used so that the contact area could be recorded with a Nikon D7100 camera body with a MX-6 lens on the InfiniMax from Edmund optics. The video was processed using Matlab code to extract the contact radius during each trial. The probes had radii of 3, 4 and 5 mm. The glass probes were coated with a conductive transparent layer of ZnO_2 so that they could be electrically connected to the voltage source. The contact area was viewed from its flat side. To prepare the glass for atomic layer deposition (ALD), it was cleaned with acetone, methanol, and isopropanol, then rinsed with DI water and air dried with N_2 gas. The TFS 500 ALD coater from Beneq was used to deposit approximately 20 nm of ZnO_2 at 150 °C. A multimeter was used to verify its conductivity; the oxide layer had a resistance of approximately 2 kΩ.

The conductive polymer layer (cPDMS) was prepared by mixing Sylgard 184, a type of polydimethylsiloxane (PDMS), with a carbon black filler from Alfa Aesar, (carbon black, acetylene, 50 % compressed). To mix the cPDMS, 7.5 wt % carbon black (relative to PDMS) was mixed with PDMS (10:1 weight ratio of base to curing agent) using the Thinky mixer. Before curing the cPDMS on a glass slide, a layer of tricholoro(octadecyl)silane from Sigma Aldrich was deposited on the slide. The layer of silane was found to be important for a smooth contact surface on the cPDMS and for easy release. To deposit a layer of silane on glass, the slide was cleaned with acetone, methanol, isopropanol, and DI water. Then it was treated in 50 W O_2 plasma using the March Jupiter III O_2 plasma system to promote adhesion. Finally, it was placed in a vacuum chamber with a few drops of silane and pumped down to 30 kPa and held there for at least 30 min. The cPDMS mixture was then poured into a mold on a the glass slide, squeegeed to a defined thickness, and cured at 60 °C for 16 h. Samples were made with thicknesses of 0.8 mm and 2.1 mm.

Once fully cured, the samples were then plasma bonded to a 7 µm thick layer of PDMS. This layer of non-conductive PDMS acted as a dielectric, electrically insulating the cPDMS from the conductive glass indenter. Plasma treatment was conducted in the Plasmod chamber at 30 W for 1 min. The thin layer of PDMS (10:1 ratio) was prepared by mixing it with hexane from Sigma Aldrich (1:1 weight ratio) using the Thinky mixer. It was then spin coated onto a glass slide that had previously been treated with silane using the same procedure described above. The spin cycle was first set to 400 RPM for 30 s to allow the solution to evenly spread over the whole slide then ramped up to 6000 RPM for 90 s. Then it was cured in an oven

at 60 °C for 16 h. This yielded a 7 µm layer of PDMS which was measured using an optical interferometer, the TMS-1200 from Polytec.

The cPDMS/PDMS layer was placed on an ITO glass slide and a voltage was applied to the ITO slide and the glass probe to generate electrostatic force, shown in Fig. 3.2. Note that the cPDMS layer is electrically connected to the ITO slide through contact so the distance between the positive and negative terminal is separated by the 7 µm thick dielectric. Tack tests, described in Sec. 3.2.1, were conducted with the glass probes contacting the soft layer. At least four trials were taken for voltages ranging from 0 V to 450 V at 150 V increments.

3.2.3 Compliant sphere, elastic half-space

The second tack system that was used to verify Eqn. 4.1 was composed of a compliant hemispherical indenter contacting an elastic half-space. The compliant probe was a cPDMS hemisphere with a radius of 4 mm and the elastic half-space was an ITO glass slide with a 7 µm thick PDMS dielectric for electric insulation. The cPDMS probe was made with the same recipe for the compliant layer discussed in Sec. 3.2.2. A negative mold made of PDMS was casted around a 4 mm glass half-ball lens from Edmund optics with a layer of silane for easy demolding. The mold was cured at 60 °C for 16 h, the glass hemisphere removed, and a layer of silane was deposited on the mold using the same procedure described in Sec. 3.2.2. Uncured cPDMS was pressed into the PDMS mold, degassed to remove air bubbles, and cured at 60 °C for 16 h. Then it was demolded and plasma bonded to a ITO glass slide and mounted

onto the end of a cantilever beam. The contacting surface (ITO glass) was electrically insulated by spin coating a 7 µm thick layer of PDMS on top of the ITO, using the same spin recipe described in Sec. 3.2.2.

3.3 Results and Discussion

3.3.1 Rigid sphere, elastic half-space

Fig. 3.4 shows the load versus time of a tack test for an aluminum sphere contacting an ITO glass slide. Within the force resolution of mNs, without an applied voltage, adhesion could not be detected between the rigid surfaces, Fig. 3.4A. With an applied voltage adhesion can be detected, showing that the tack force measured in this system is dependent only on electrostatics. The tack force (P_c), at point C in Fig. 3.4B, can be plotted as a function of applied voltage squared, shown in Fig. 3.5. It is clear that P_c scales with V^2 and can be predicted by Eqn. 3.7. This demonstrates that Eqn. 3.7, which is for the non-contact, long range electrostatic force, can be used to estimate the adhesive force due to electrostatics, such that, $P_c = P_v$.

For an elastic half-space where $R >> a$ only the tack force and probe radius is necessary to calculate the driving force for fracture, Eqn. 3.5. Fig. 3.5 can be replotted in terms of the driving force for fracture, displayed in Fig. 3.6. The figure shows that G_c scales with V^2, and this relationship can be predicted by Eqn. 3.8.

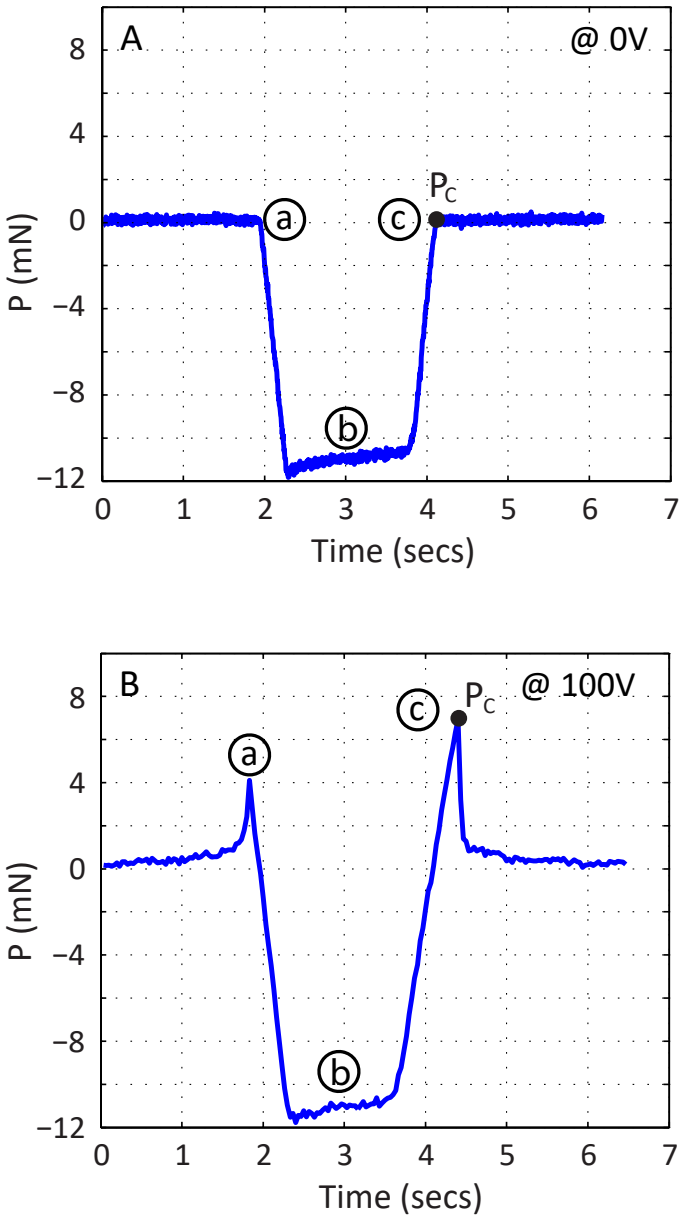

Figure 3.4: A) Example of the force experienced by the rigid aluminum probe over time. A) Shows the force over time of a JKR tack test without an applied voltage. The loading phase (a) is when the probe approaches the glass slide at 10 µm/s until contact and a mechanical preload (b) of 6.0 mN. The probe is then unloaded at the same speed until contact is broken (c). The force recorded when contact is broken is attributed to the adhesive force due to electrostatics, in this case, zero. B) Demonstrates the force experienced when 100 V was applied to the probe. Here an initial increase in force before contact is due to electrostatics. The peak, P_c, observed at (c) is considered to be the tack force due to an applied voltage.

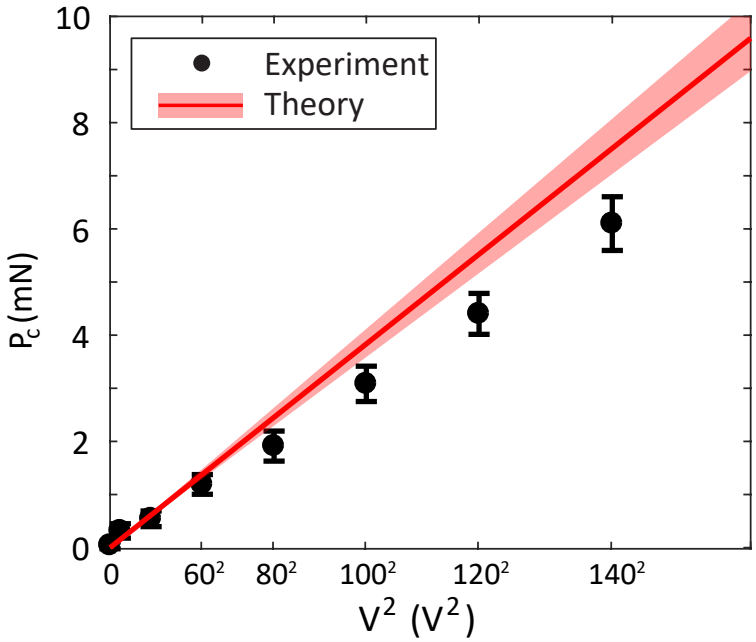

Figure 3.5: Tack force plotted against the applied voltage squared for a conductive sphere contacting a rigid ITO glass slide. The theory line is based on Eqn. 3.7 and the shaded area is the error due to a 0.1 µm uncertainty in the dielectric thickness. This an average of data taken from two identical spheres tested at least three times at each applied voltage.

3.3.2 Charging and dielectric breakdown

When using electrostatic force, the magnitude of the applied electric field and the dielectric material's propensity to store trapped charges can cause a buildup of charge in the dielectric layer. Charging will reduce electrostatic force through a secondary opposing electric field and thereby, lower the measured tack force. Consecutive trials with an applied voltage of 100 V were carried out to test if charging effects were present in this system. As seen in Fig. 3.7, with 16 consecutive trials without any break between each, the tack force did not reduce. Additional precautions were taken to prevent charging by randomizing the order of the applied voltage; this prevented charging from becoming a systematic error.

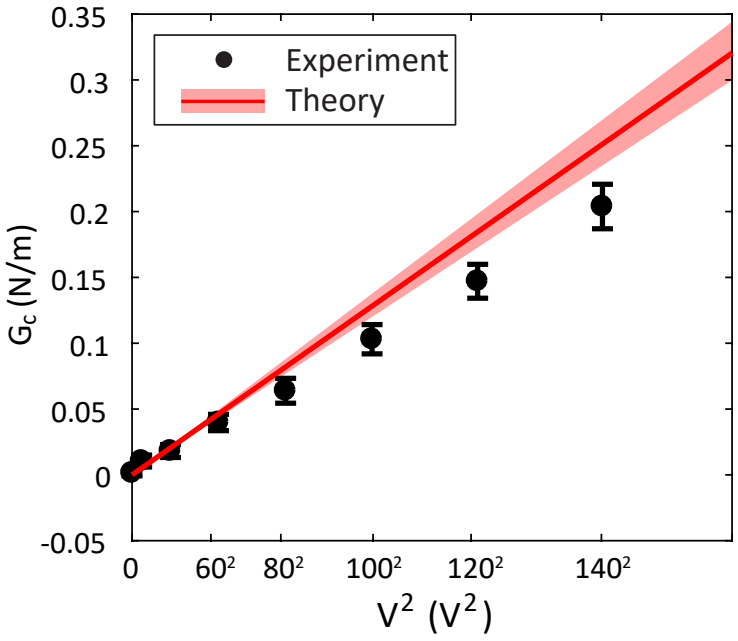

Figure 3.6: Critical energy release rate calculated from the tack forces in Fig. 3.5 plotted as a function of the applied voltage squared. The theory line is based on Eqn. 3.8 and the shaded area is the error due to a 0.1 µm uncertainty in the dielectric thickness.

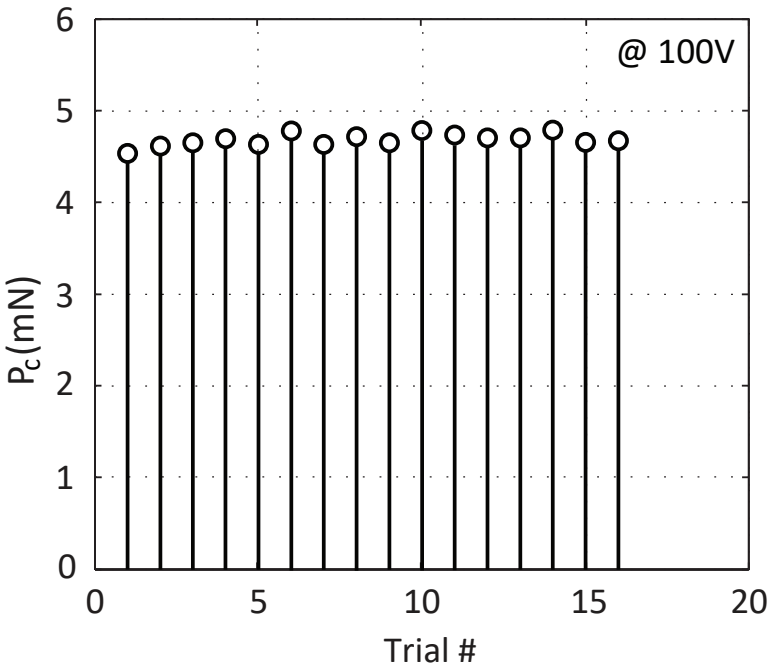

Figure 3.7: Repeated tack tests with a metal probe at 100 V with a dielectric thickness of 1.5 µm. There was no wait time between each trial

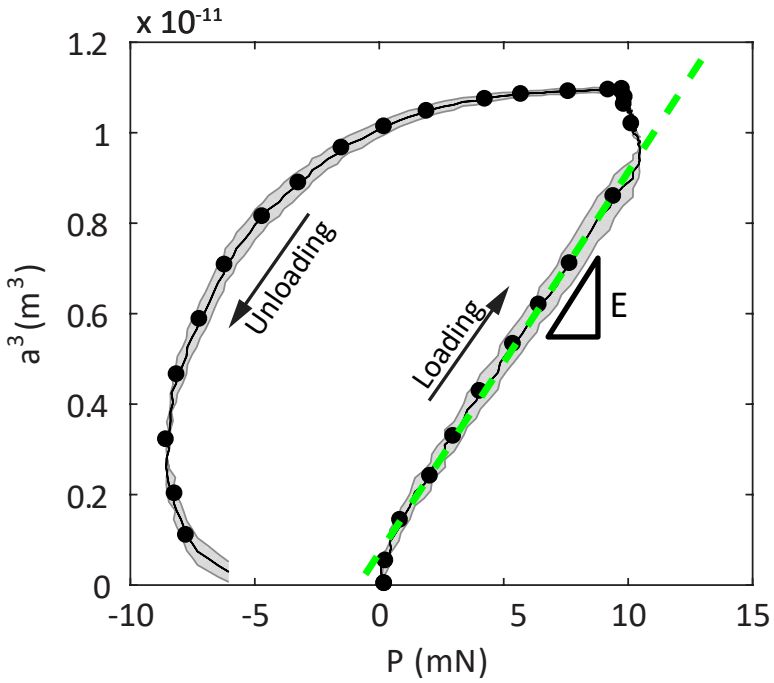

Figure 3.8: Example of a JKR tack test without an applied voltage.

With electrostatic force, the range of G_c can be actively tuned by varying the applied voltage. The lower limit of G_c (i.e. $V = 0\,\mathrm{V}$) is set by the adhesive property of the compliant layer and the upper limit, on the breakdown voltage of the dielectric. At breakdown voltage, electrical insulation fails and a current passes through the dielectric between the conductive surfaces, without a voltage difference, electrostatic force disappears.

3.3.3 Validity of linear elastic assumption

Fig. 3.8 shows the loading and unloading cycle of a JKR tack test without an applied voltage for a rigid glass probe contacting a conductive elastomer layer. It was observed that the slope of the loading cycle is linear, indicating that the linear elastic assumption necessary for the JKR theory was valid for this adhesive system.

The elastic modulus of the compliant layer can be estimated with Eqn. 3.16, which assumes that during loading, adhesive forces are turned "off", and the relationship between the measured load and contact radius cubed can be described by the Hertz equation for contact between a sphere and elastic half-space.

$$P = \frac{16Ea^3}{9R} \tag{3.16}$$

The elastic modulus is obtained by adjusting the modulus to get the best fit between Eqn. 3.16 and the loading curve. An average elastic modulus of 3.6 MPa was obtained.

With the estimated modulus at 0 V and the measured load and contact radius, the energy release rate can be calculated with Eqn. 3.10 for all points during the tack test. The energy release rate is plotted against the contact radius in Fig. 3.9. During the loading cycle, G is constant and then begins to rise as unloading starts. It reaches the critical energy release rate at which the crack begins to propagate and the contact radius decreases. G continues to increase as the crack propagates due to viscoelastic dissipation at the crack tip. The constant G_a during the loading phase for tack tests without an applied voltage is approximately 0.004 N/m.

3.3.4 Driving force for interfacial fracture

The tack tests for different applied voltages are shown in Fig. 3.10. Applying an electrostatic force into the system increases the contact radius before fracture occurs; a maximum increase of 80 µm in contact radius was observed. The force experienced by the probe at the beginning of loading is tensile due to electrostatic attraction.

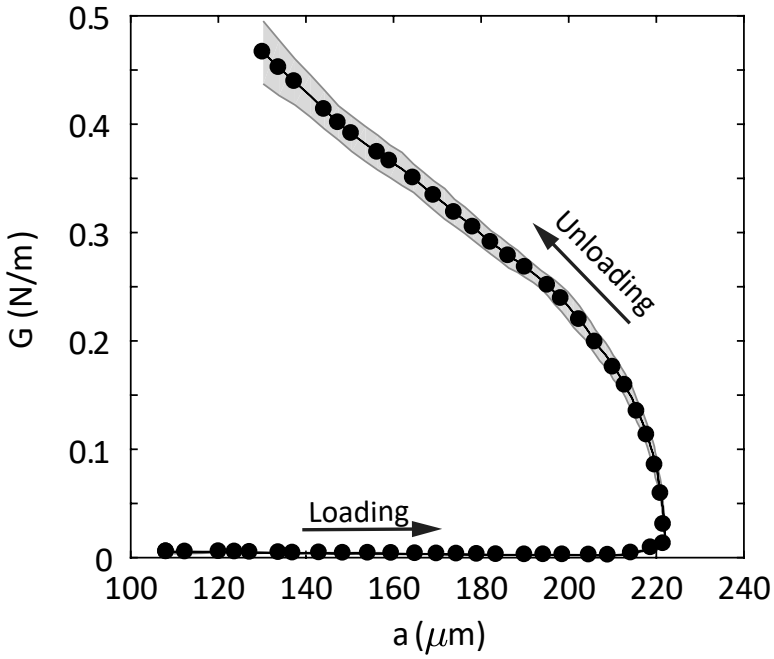

Figure 3.9: Example of a JKR tack test plotted in terms of energy release rate versus contact radius without an applied voltage. G during loading is constant while for unloading it increases due to viscoelastic dissipation.

Despite increasing initial tensile force between the surfaces prior to contact, all tests reached the same mechanical preload of 10 mN. The slope of the loading curve also increased with voltage, this corresponds to a lower estimated elastic modulus. This will be addressed later in Sec. 3.3.6.

G_c was determined for tack tests with different probe radii and compliant layer thicknesses at different applied voltages. Fig. 3.11 shows that G_c scales with V^2 for different probe radii on a 2.1 mm thick compliant layer. The driving force for fracture due to the polymer's adhesive properties, G_o, is approximately 0.02 N/m. By applying an electrostatic force, the driving force for fracture of the whole system, G_c, which includes the effect of polymer adhesion, increased to 0.2 N/m at 450 V, a 10x improvement. A higher G_c could be achieved with larger applied voltages,

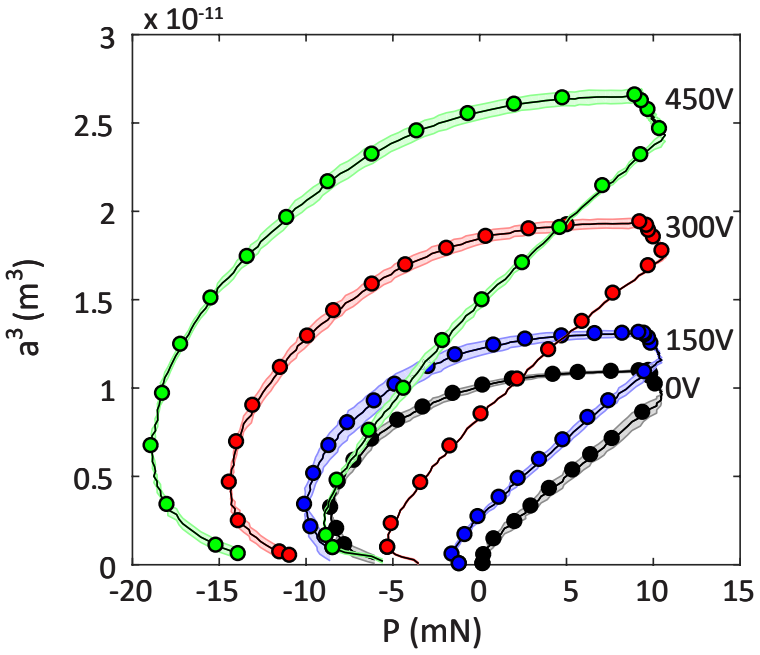

Figure 3.10: Example of JKR tack tests different applied voltages with a 5 mm radius probe on a 2.1 mm thick compliant layer. The color bands indicate the standard deviation of at least 4 trials at each applied voltage. The initial force at the start of the tack test shifts towards tensile force (negative) with increasing voltage because of electrostatic attraction. Before contact, there is electrostatic attraction between the probe and substrate which pulls on the cantilever beam, registering a initial tensile force at contact. A mechanical or compressive preload of 10 µN is kept the same for all the experiments, regardless of the initial tensile force.

however, voltages larger than 450 V had a higher rate of dielectric breakdown.

A linear fit of the experimental data, using G_o =0.02 N/m as a constant, shows that Eqn. 3.15 can be used to predict the driving force for fracture with a non-dimensional fitting parameter, $c_1 = 0.38$, modifying G_v. This fitting parameter, however, is not specific to this set of experimental data. Instead of varying the probe radius, a 4 mm glass probe was used to contact compliant layers with a thicknesses of 0.8 mm and 2.1 mm, shown in Fig. 3.12. A second tack system with a 4 mm compliant probe contacting an ITO glass slide is also plotted in the same figure, green stars. A

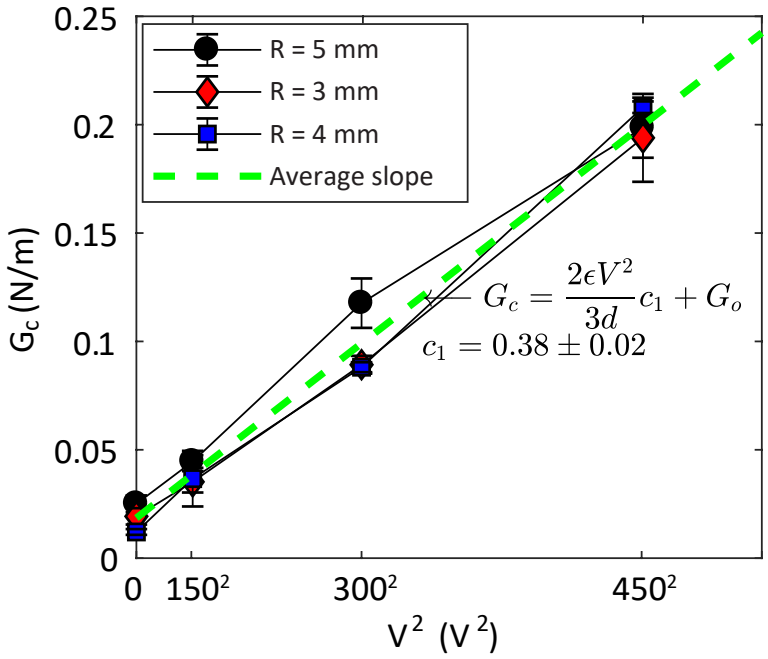

Figure 3.11: Critical energy release rate as a function of applied voltage squared for varying probe radius on a 2.1 mm thick cPDMS layer. The PDMS dielectric was 7 µm thick. The green dash line is a linear fit of the experimental data with G_o as the average $G_c|_{V=0}$ =0.03 N/m, i.e. the driving force for fracture due to polymer adhesion.

linear fit of the experimental data with a constant G_o =0.02 N/m in Eqn. 4.1 yields the same fitting factor of $c_1 = 0.37$.

The superposition of electrostatic and polymer adhesion on critical energy release rate was demonstrated with different probe radii, compliant layer thicknesses, and a secondary tack system. And the contribution of electrostatic to the driving force for fracture in elastomers can be predicted by $G_v * c_1$ where $c_1 = 0.38$.

3.3.5 Driving force for receding cracks

Electrostatic force does not just affect the driving force for interfacial fracture; it can be observed from Fig. 3.14 that electrostatics also affect the energy release rate for

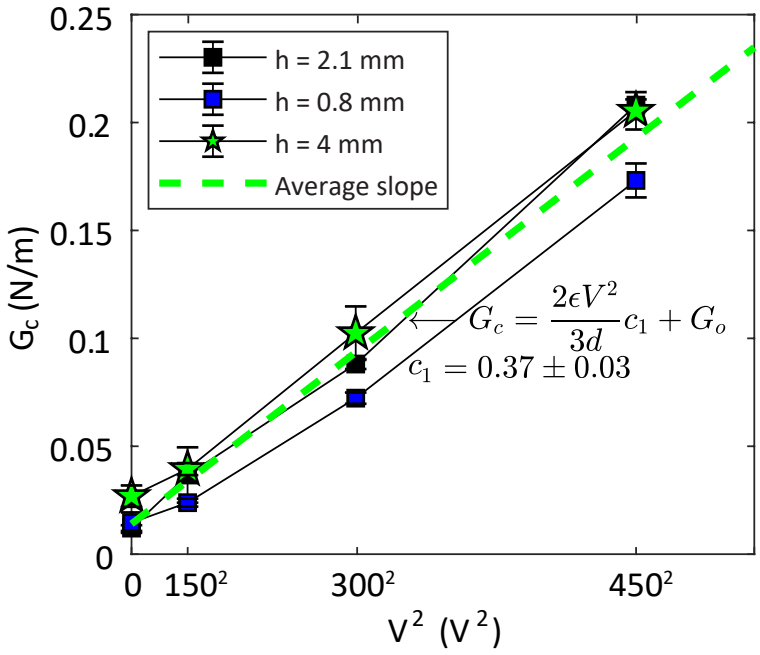

Figure 3.12: Critical energy release rate as a function of applied voltage squared for varying compliant layer thicknesses with 4 mm radius glass probes, circular dots. The green stars are experimental data from a 4 mm radius cPDMS probe contacting an ITO glass slide with a 7 µm thick PDMS dielectric. The green dash line is a linear fit of the experimental data with G_o as the average $G_c|_{V=0}$ =0.03 N/m.

a receding crack (loading cycle). A constant G_a can be calculated from Fig. 3.14 by averaging G during the mechanical loading portion of the cycle. It is assumed that the thermodynamic work of adhesion and viscoelastic dissipation during a receding crack remain constant for different applied voltages, called $G_w = G_a|_{V=0V}$. Previously, it was shown that the contribution of electrostatic force to the critical energy release rate can be expressed as a superposition of the different adhesive mechanisms, implying that electrostatic force is independent of polymer adhesion. G_a, then, may also be a superposition of G_w and G_v. Fig. 3.14 plots the relationship between G_a and V^2.

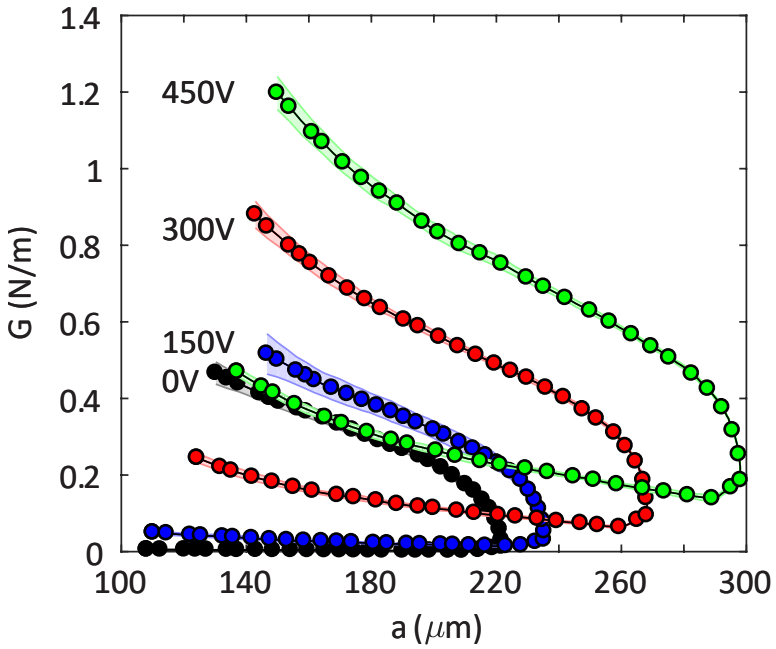

Figure 3.13: Example of a JKR tack test plotted in terms of energy release rate versus contact radius without an applied voltage. G during loading is constant while for unloading it increases due to viscoelastic dissipation.

G_w was measured to be 0.02 N/m. Plotting the modified Eqn. 4.1 such that

$$G_a = G_w + G_v c_1 \tag{3.17}$$

where G_o is replaced with G_w and G_c with G_a, the theory line is a good match with the experimental data. This shows that the effect of electrostatic force on energy release rate is constant during a JKR tack test and can be quantified by Eqn. 3.8.

3.3.6 Elastic modulus

Earlier it was noted that the slope of the JKR loading curve, Fig. 3.10, changes with voltage. A modulus based on that slope can be obtained using Eqn. 3.11 and plotted against voltage, black points. Eqn. 3.11 assumes that adhesive forces are turned off

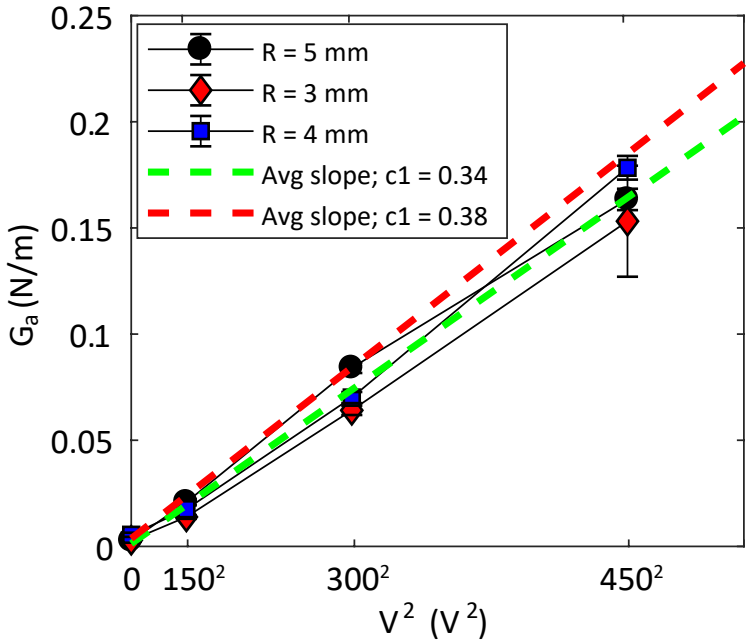

Figure 3.14: Relationship between the energy release rate for a receding crack and the applied voltage squared. The red dashed line is the linear fit based on the experimental data in Fig. 3.12 with a fitting factor, c_1, of 0.38. The green dashed line is the linear fit based on the average G_a during the loading phase with a fitting factor, c_2, of 0.34.

and clearly, as shown earlier, electrostatics affects the energy release rate during the loading cycle. However, since the effects of electrostatic are constant during a receding crack and can be quantified by Eqn. 3.8 then its contribution can be eliminated by subtraction and the energy release rate due to polymer adhesion can be recovered. The following expression is used to isolate the energy release rate due to polymer adhesion, assuming a constant G_a:

$$G_w = G_a - G_v c_1 \tag{3.18}$$

G_w can then be inserted into a rearranged version of Eqn. 3.10 to calculate the load for when no electrostatic force is present.

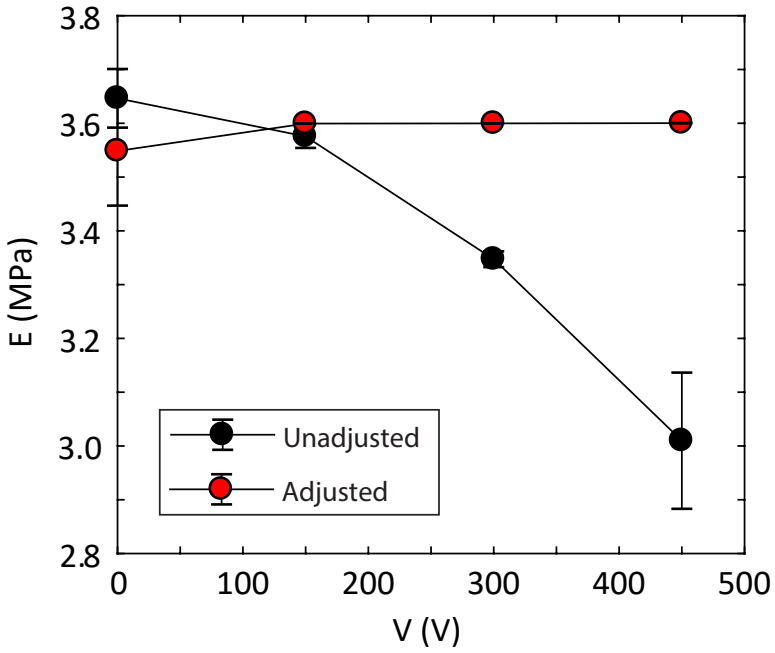

Figure 3.15: Effect of electrostatic force on the loading curve described with the estimated elastic modulus as a function of applied voltage. The black circles are the estimated elastic modulus based on the experimental data without any modifications. The red circles are the adjusted modulus from the calculated the load which was based on the energy release rate data with the contribution of electrostatic force subtracted.

$$P = P' - \left[\frac{(G - G_v)Ea^3B^{-1}}{0.022}\right]^{1/2} \tag{3.19}$$

where $B = \frac{0.75+2(a/h)+4(a/h)^3}{(0.75+a/h+(a/h)^3)^2}$. The elastic modulus at 0 V is used and the contact radius used to calculate G was kept the same. Loading portion of the JKR tack test without an applied voltage can be recovered, and the newly estimated elastic modulus of the estimated P and a^3 plot is shown in Fig. 3.15 as red dots. The change in modulus is due to electrostatic force and not a change in the material property of the compliant layer.

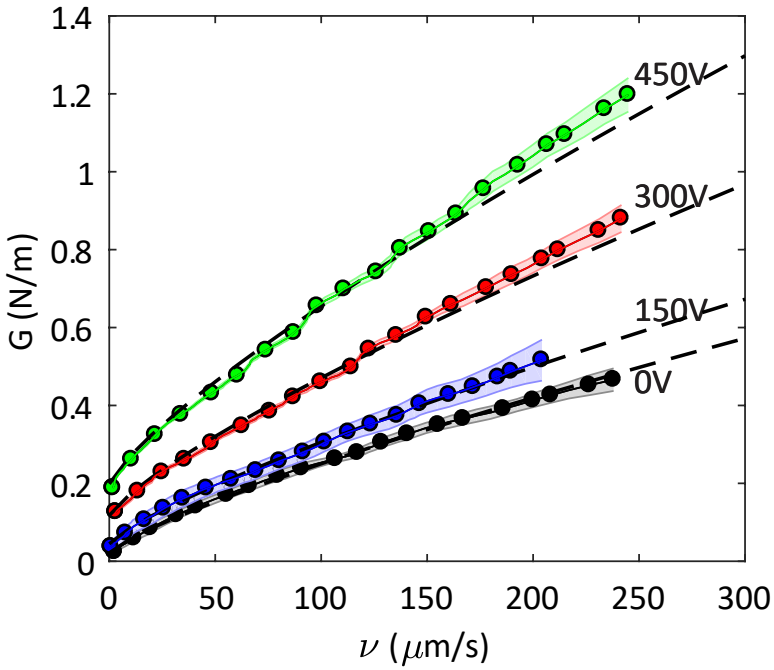

Figure 3.16: Effect of electrostatic force on the relationship between energy release rate and crack velocity, for a 5 mm radius glass probe contacting a 2.1 mm thick compliant layer. The dashed black lines are the predicted curves using Eqn. 3.12 with $n = 0.8$ and varying to v^* to obtain the best fit curve with linear regression.

3.3.7 Energy release rate for advancing cracks

The change in energy release rate during crack propagation is affected by viscoelastic dissipation at the crack tip, which is velocity dependent. The energy release rate can be plotted against the speed at which the crack propagates during stable fracture, Fig. 3.16. G_c is the value of G right before fracture begins. While Eqn. 3.8 can explain the increase in G_c due to an applied voltage, it does not account for the change in slope of the energy release rate compared to crack velocity.

The effect of electrostatics on the kinetics of crack propagation can be examined by fitting Eqn. 3.12 to the experimental data in Fig. 3.16. The best fit for the material parameter, n, at 0 V was 0.8. To fit the experimental data with an applied voltage,

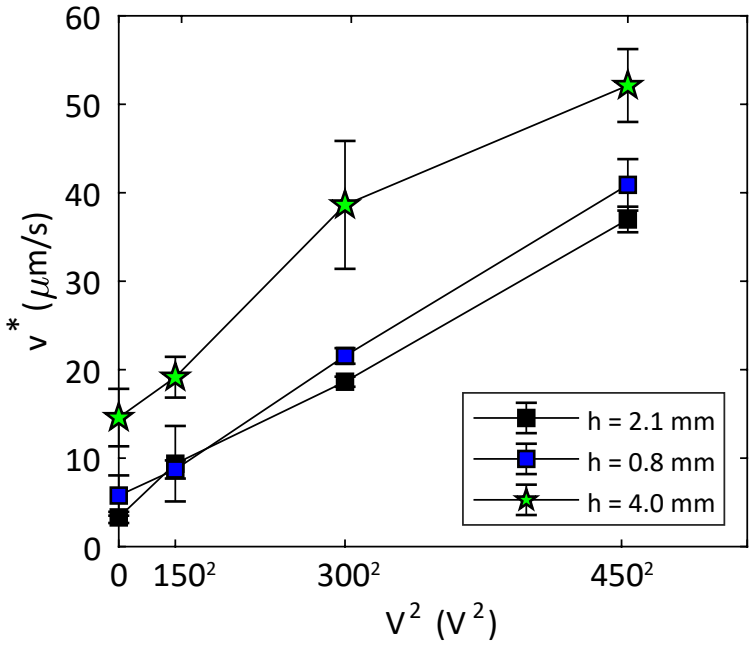

Figure 3.17: Effect of electrostatic force on the relationship between the characteristic velocity and applied voltage squared. This contains data from 4 mm radius glass probes contacting compliant layers with 0.8 mm and 2.1 mm thicknesses and a 4 mm radius cPDMS probe contacting an ITO glass slide.

$n = 0.8$ was kept constant and the characteristic velocity, v^*, was varied to obtain the best fit for the relationship between energy release rate and crack velocity, shown as the dashed lines in Fig. 3.16.

Fig. 3.17 reveals that the characteristic velocity scales with V^2. For small scale viscoelasticity, where viscoelastic effects are present only near the crack front, v^* is a function of the characteristic stress relaxation time (t^*) of the compliant layer and the length of the cohesive zone (z), expressed as $v^* = z/t^*$. The characteristic stress relaxation time can be calculated by measuring the time it takes the polymer to reach 63.5% of the steady state stress in a creep test with a constant strain. A constant strain creep test was conducted on a cPDMS ASTM 412 dogbone sample scaled down by a factor of 4. The characteristic stress relaxation time was 3.6 s over 3 trials. The

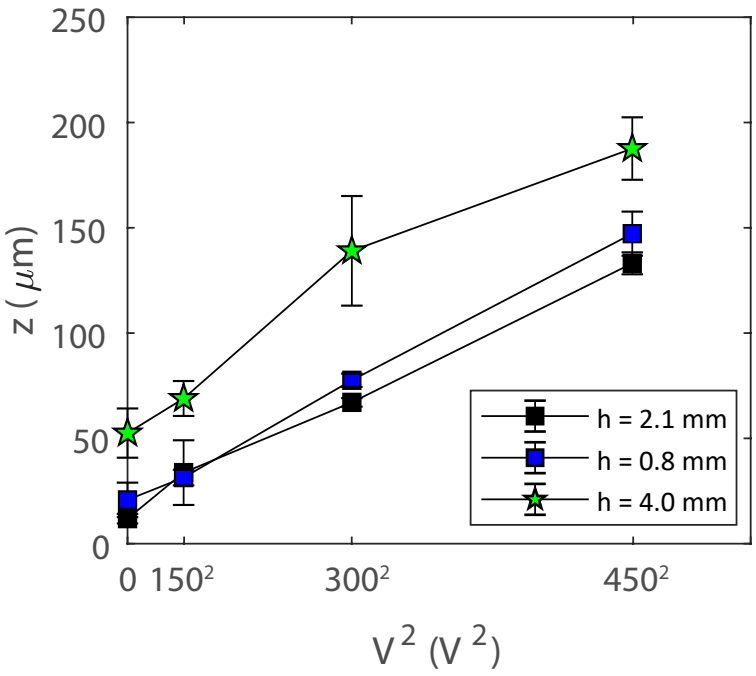

Figure 3.18: Effect of electrostatic force on the cohesive zone with a characteristic relaxation time of 3.6 sec.This contains data from 4 mm radius glass probes contacting compliant layers with 0.8 mm and 2.1 mm thicknesses and a 4 mm radius cPDMS probe contacting an ITO glass slide.

cohesive zone can be plotted against V^2, Fig. 3.18, showing that electrostatic force expands the effective cohesive zone around the contact area, requiring more energy to propagate fracture.

These results prove the hypothesis that critical energy release rate of a polymer-based electroadhesive can be described as the superposition of polymer adhesion and electrostatics. Additionally, the effect of electrostatic force on the characteristic crack velocity can be attributed to the expansion of the cohesive zone, and its relationship with voltage can be characterized by experimental data. The mechanics of adhesion and detachment for spherical electroadhesives can be fully predicted by using Eqn. 3.15 and Eqn. 3.12 for any voltages. These models will be useful for understanding

the deformation behavior of electroadhesives; however, additional work is necessary to translate these findings into real world applications.

Chapter 4

Textured Electroadhesives

Polymer-based electroadhesion and gecko adhesion have been developed over the years to address similar applications, such as, pick and place, climbing robots, and grasping [1, 12, 14, 27]. Gecko adhesives, also called dry adhesives, use the inherent stickiness of a polymer to attach to surfaces, and often times use fribrillar features to improve compliance to surfaces and enhance adhesion [12, 17, 40].

Soft electroadhesives use stretchable conductive polymers to adhere to surfaces through electrostatic force [4, 20, 26]. The adhesives are made of soft elastic polymers because their compliance can help obtain close contact with surfaces in order to ensure a high electrostatic force. Because soft electroadhesives are made of polymers, the inherent stickiness of the material contributes to the total adhesion of the electroadhesive. This naturally leads to ideas of combining dry adhesives with electrostatics.

While dry adhesives have shown that they are able to achieve high adhesive force for small contact areas and are robust in real world applications, they are limited by the fixed stickiness of their surface. They have no ability to increase or decrease the adhesion of their surface; once attached, they can only turn it "off" through their detachment mechanism. Their adhesion also does not scale easily in overall device size because of difficulty in aligning fibrillar arrays and engaging all fibers during the preloading stage [40]. Electroadhesion can be instantaneously adjusted by

varying the applied voltage. And electrostatic force can provide additional electrical preload to improve contact, which may help improve the scaling of dry adheisves. By combining dry and electroadhesives, it is possible to increase the maximum adhesion force, improve contact, and give the ability to tune the stickiness of the device.

There has been some work done to combine the two adhesive mechanisms [27, 41–43, 72]. In Ruffatto, their device has a fribillar layer for dry adhesion and a backing layer with electrodes that apply electrostatic force [27, 41]. Krahn also uses a similar stacking method in their EDA device [43]. These papers have demonstrated that the electrostatic layer provides an additional electrical preload to increase contact between the surface and the dry adhesive layer. Ruffatto demonstrated that this increased the maximum load their device can hold on a variety of surfaces by up to 5x greater on some surfaces. These work done to integrate soft EA and dry adhesion resulted in applied voltages in the thousands due to this stacking method. The dry adhesive layers are usually tens of microns thick which subsequently requires thousands of volts to generate sufficient electrostatic force.

Here, we present a simple fabrication process and design framework which create electroadhesives that can operate at hundreds of volts instead of thousands while increasing the range of controllable adhesion through textured surfaces and multi-tiered contact areas. We were able to achieve an increase of adhesion up to 20x. We also attach textured electroadhesives to a Kuka iiwa robot arm to demonstrate the potential for pick and place applications. Sec. 4.1 lays out the equations used to calculate electrostatic force and its relation to contact splitting. Sec. 4.2 describes the fabrication process and experimental setup and Sec. 4.3 goes over the results of

the tack tests and discuss their implications. Application of the soft electroadhesives are shown in Sec. 4.3.4.

4.1 Theory

4.1.1 Spherical Probe

It was shown in Chapter 4 that electrostatic force and polymer adhesion act as independent adhesive forces which can be described by the following equation:

$$P_c = P_o + P_v \tag{4.1}$$

where P_c, measured in a tack test, can be separated into two force terms: P_o, the nominal tack force where there is no electrostatic force present, and P_v, the electrostatic force. Tack force is not an intrinsic property and can change based on experimental parameters, such as but not limited to, unloading speed, type of contacting surface, preload, and radius of the probe. While tack force is not a parameter that can be directly compared between different tack systems, it can give an estimate of the real force an adhesive can withstand.

For a polymeric spherical probe contacting an elastic half space, Fig. 4.1A, where the contact radius is significantly smaller than the probe's thickness ($a/h \to 0$), the tack force can be calculated based on the following JKR equation,

$$P_o = \frac{3}{2}\pi R G_o \tag{4.2}$$

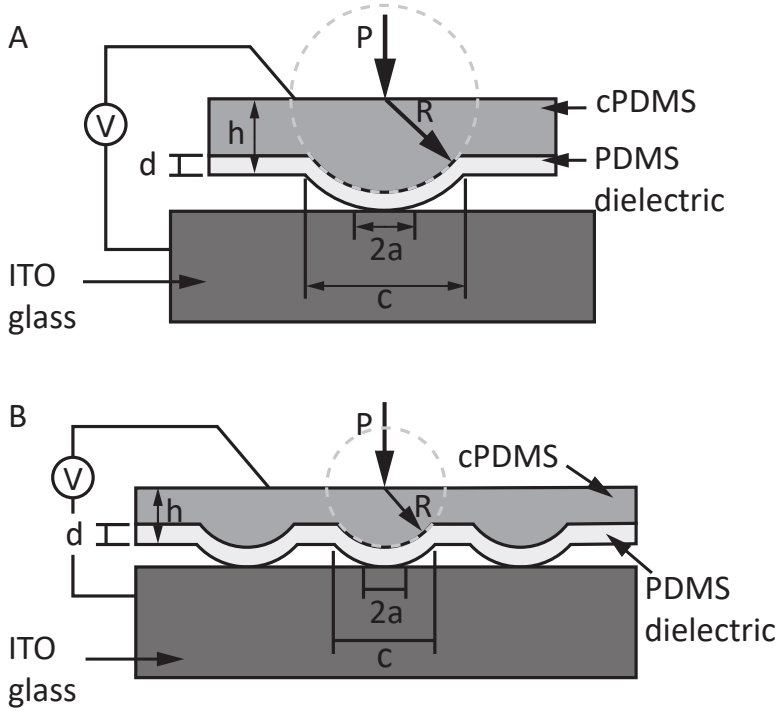

Figure 4.1: Schematic of a textured electroadhesive contacting a conductive surface. A) R is the radius of the sphere, P is the measured load on the probe, a is the contact radius, h is the height of the probe, and d is the diameter of the probe. B) The bumps are sections of a larger sphere where R is the radius of curvature, c is the chord length, h is the height, and d the dielectric thickness.

where R is the radius of the sphere and G_o is the critical energy release rate of the polymer.

The electrostatic force between a conductive sphere and conductive plate, as described by Crowley [71], can be approximated as

$$P_v = \frac{\epsilon \pi R V^2}{d} \tag{4.3}$$

where $\epsilon = \epsilon_0 \epsilon_r$ and ϵ_0 and ϵ_r are the permittivity of free space and the dielectric constant of the insulating layer, respectively, v is the applied voltage, and d is the distance between the sphere and plane, and in the case of contact, the dielectric thickness.

The total tack force of a conductive sphere contacting an elastic half space can be written as a combination of Eqn. 4.2 and Eqn. 4.3 to get the following,

$$P_c = \frac{3}{2}\pi R G_o + \frac{\epsilon \pi R V^2}{d} \tag{4.4}$$

Eqn. 4.4 shows that the total tack force is a function of the spherical probe's radius, and increasing the radius will increase electrostatic force. A range of tack forces can be obtained by controlling for the applied voltage, with the floor being P_o and the ceiling, $P_{vmax} + P_o$, where the electrostatic force P_{vmax} depends on the maximum voltage that can be applied without dielectric breakdown. A ratio can be used to evaluate the adhesion range of a particular electoradhesive by dividing the maximum electrostatic force with the nominal tack force, P_{vmax}/P_o. This gives a measure of

how high the ceiling is for the controllable adhesion range relative to the floor.

4.1.2 Multiple Spheres

A single probe cannot hold much force even with electrostatics and a large radius. However, the range can be further improved by adding more spherical contacts, referred to as bumps, shown in Fig. 4.1B. Gecko adhesives have long used arrays of pillars to improve adhesion and contact for uneven surfaces; and it has been shown that for arrays with spherical contacts, the tack force increases at a $n^{1/2}$ rate [17]. For this paper, the array of bumps are sections of larger spheres, where the bumps have the same radius of curvature, R, of the spheres, so that Eqn. 4.4 can still be used.

Since, electrostatic force is independent of polymer adhesion and assuming the distance between the bumps are large enough that the electric fields at each bump are independent of each other, it is hypothesized that the electrostatic force increases linearly with the number of bumps. The total tack force for an array of bumps can then be written as,

$$P_c = n^{1/2} P_o + n P_v \tag{4.5}$$

Eqn. 4.5 shows that even though the nominal adhesion will increase with the bump array, electroadhesion will increase at faster rate. The controllable adhesion range can be written as the following,

$$\frac{P_{vmax}}{P_o} \approx \frac{\epsilon V^2}{G_c} n^{1/2} \tag{4.6}$$

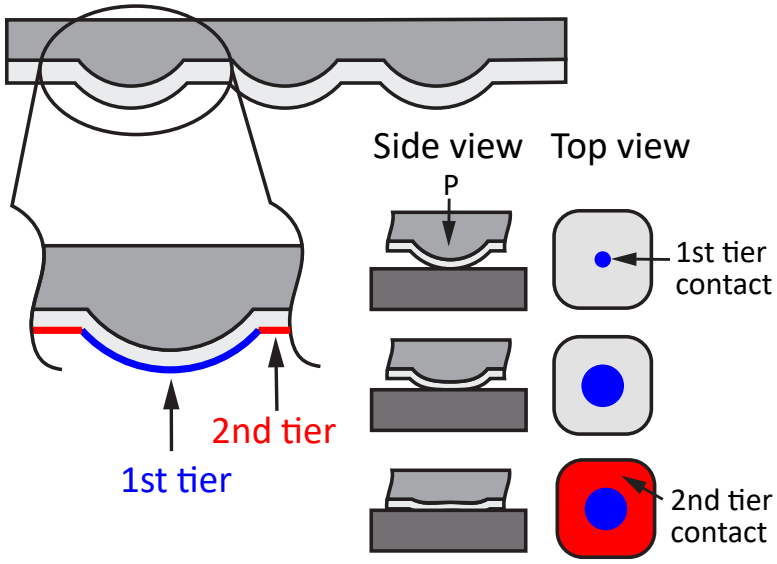

Figure 4.2: Schematic of a multi-tiered textured electroadhesive contacting a conductive surface. The first tier area is the spherical bump, highlighted in blue. The second tier area is the area around the bump, highlighted in red.

which reveals that the range can be extended by simply increasing n.

4.1.3 Pull-in effect

Another electroadhesive design that can increase the range of forces is by fabricating devices with multi-tiered contact areas. This can be achieved by using the same textured structures shown previously, but adjusting the height between the 1st and 2nd tier areas, Fig. 4.2. Adhesion for the 1st tier is governed by the array of bumps and can be predicted by Eqn. 4.5. However, as the electrostatic force increases and the distance between the 2nd tier area and the contacting surface shrinks, there is a voltage threshold where instability occurs and the gap closes. This effect is commonly called the pull-in effect and is often observed in electrostatic gap actuators.

Once the 2nd tier pulls-in and contacts the surface, the contact area is no

longer in the form of an array of circular areas and Eqn. 4.5 cannot be used to predict electroadhesion. The electrostatic equation depends on the design of the 2nd tier area. The area could be a second array of spherical bumps or flat pillars. However, in this paper, the 2nd tier area is the area around the array of bumps; so once pulled-in, the contact can be approximated as a parallel planes in contact, separated by a dielectric. The electrostatic equation for parallel plates can then be be used to estimate the force, written as

$$P_v = \frac{\epsilon A V^2}{2d^2} \tag{4.7}$$

where A is the contact area of the 2nd tier and d is the dielectric thickness.

4.2 Fabrication and Experimental Setup

4.2.1 Fabrication

Two electroadhesive designs were fabricated: a single bump device with varying radius of curvatures and an array of spherical bumps. Both devices were made from acrylic molds. Casted acrylic sheets, quarter inch in thickness, were purchased from McMaster-Carr and milled using the Roland MDX-540 Mill, Fig. 4.3. It was important to use sharp ball-end mills specialized for milling acrylic and to set the tool path intervals and cut-in amount to 10 µm to ensure a smooth mold. After milling the molds, they were vapor polished with acetone. Vapor polishing was done by evaporating acetone on a hot plate in a closed glass container with the mold inside.

The same process detailed below was used to fabricate both electroadhesive designs, shown in Fig. 4.3. The conductive polymer, cPDMS, was made according to the recipe described in Chapter 3.2.2, then mixed with hexane at a 1:2 weight ratio. The polymer-solvent solution was mixed in the Thinky 310 for 1 min at 2200 RPM. The solution was then pipetted into the acrylic molds and degassed. The cPDMS was mixed with a solvent in order to reduce the viscosity of the polymer so that air bubbles would not form in the cured device or near the surface of the mold. This was an issue for electroadhesives that had a large bump array, since the small bumps would trap air bubbles when the cPDMS was too viscous. After degassing, the polymer-solvent solution was cured in the oven at 80 °C for at least 10 min to evaporate the solvent and cure the cPDMS. The solvent added volume to the polymer mixture, but after it evaporated the amount of polymer left in the mold did not fully fill it. So a second layer of uncured cPDMS, without any solvent, was spread on top of the partially filled mold and sandwiched with a silanized glass slide. It was then cured in the oven at 80 °C for at least 30 min.

After curing, the electroadhesive was released from the mold and a PDMS dielectric layer was spin-coated on top. The PDMS was made with a 10:1 base to curing agent ratio and then mixed with hexane at a 1:1 weight ratio. The polymer-solvent solution was poured on top of the electroadhesive and spun in the WS-400BZ spin coater by Laurell. A two-step spin cycle was used; first, it was spun at 400 RPM for 30 sec to spread the PDMS/hexane across the entire surface of the electroadhesive, then spun at 6000 RPM for 1 min to obtain a thin layer of PDMS. The device was then cured in the oven at 80 °C for 12 hr. A 6 µm thick PDMS was measured on a

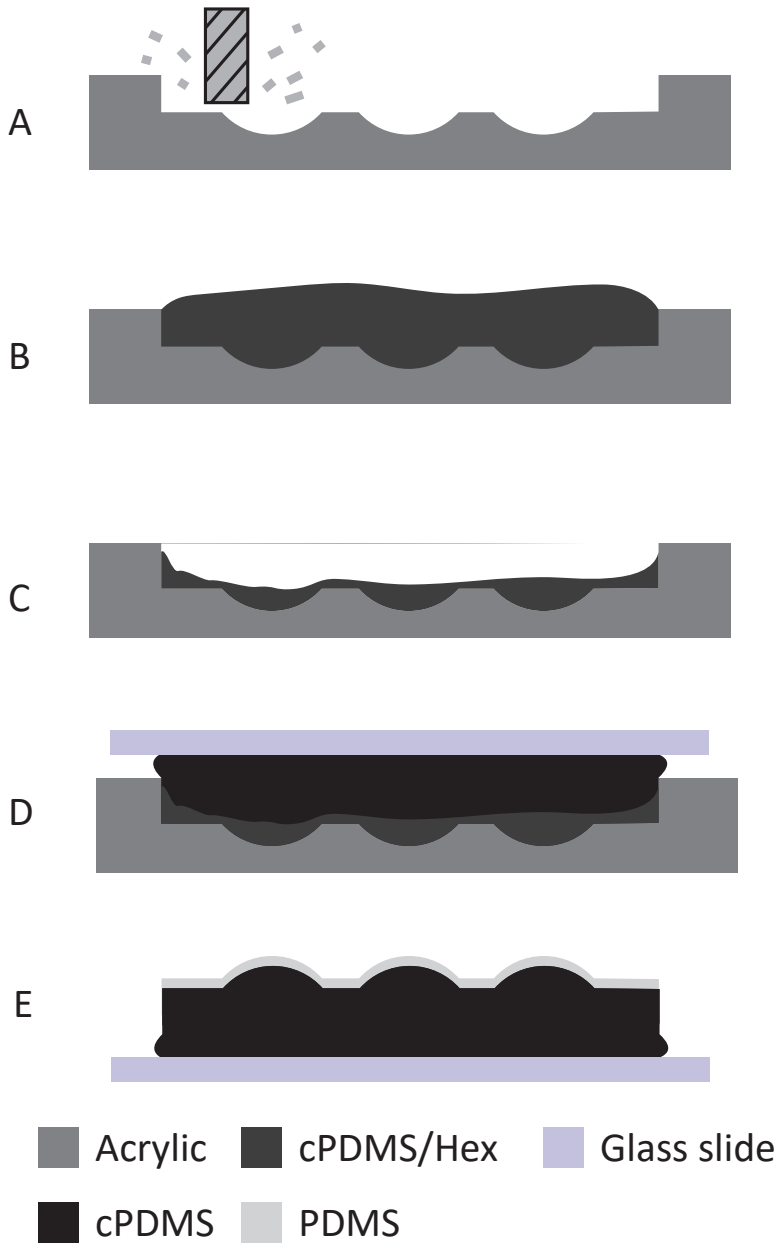

Figure 4.3: Fabrication process for a textured electroadhesive. A) The acrylic mold was milled in the Roland MDX-540. B) Then mold was vapor polished with acetone and the cPDMS/hexane mixture was poured into the molds. C) The mixture was degassed and cured at 80 °C. D) Another layer of cPDMS without solvent was spread on top of the partially filled molds and sandwiched with a silanized glass slide and cured at 80 °C. E) The textured device was then removed and a thin layer of PDMS/hexane was spin coated on top of the device and cured at 80 °C for at least 16 h.

curved bump using the confocal microscope, the LSM 800 by Zeiss.

4.2.2 Experimental Setup

To evaluate the effect of different curvatures and number of bumps on adhesion, the same tack test setup described in Chapter 3 was used. The electroadhesives were mounted onto an ITO glass slide, attached to the end of an acrylic cantilever beam with a moment arm of 35 mm. Since the electroadhesives were manually placed on the ITO, the actual position of the force applied along the moment arm shifted. Therefore, before every experiment, known weights were placed on top of the electroadhesive to calculate the true length of the moment arm. The single bump devices were mechanically loaded to 10 mN at 3 µm/sec and unloaded at 6 µm/sec. A slower loading speed was used so that the preload force would not significantly exceed 10 mN. The loading speeds were the same for the bump arrays, however, the preload was varied such that it was 10 mN times the number of bumps in the array, e.g. a 3x3 array had a 90 mN preload. Tack tests were done at least 3 times for each voltage from 0 V to 400 V at a 100 V increments for both the single bumps and bump arrays. After every set of voltage tests, the sample was discharged using the Staticmaster 2U500 from Thomas Scientific.

Aligning the textured EA to be parallel to the contacting ITO slide was important to obtain accurate measurement of the tack force. Misalignment caused the force to be unevenly distributed across the array, so that certain bumps were in contact while others were not. A yaw-pitch stage from Thorlab was used to manually adjust

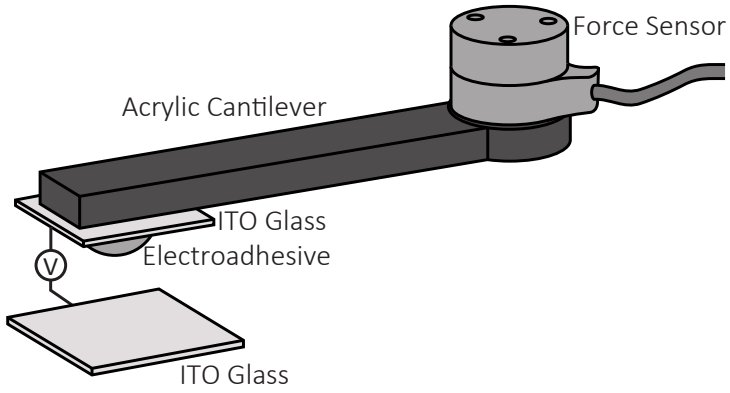

Figure 4.4: Schematic of the experimental setup. An electroadhesive is attached to an ITO glass slide on the end of an acrylic cantilever beam. The beam is attached to a 6-axis force sensor that measures the torque exerted. The force sensor is connected to a linear motor that moves the sensor and cantilever beam vertically to bring the electroadhesive in and out of contact with the ITO glass. The linear stage is connected to a yaw/pitch stage that is manually adjusted so that the surface of the textured device is parallel to the ITO glass slide.

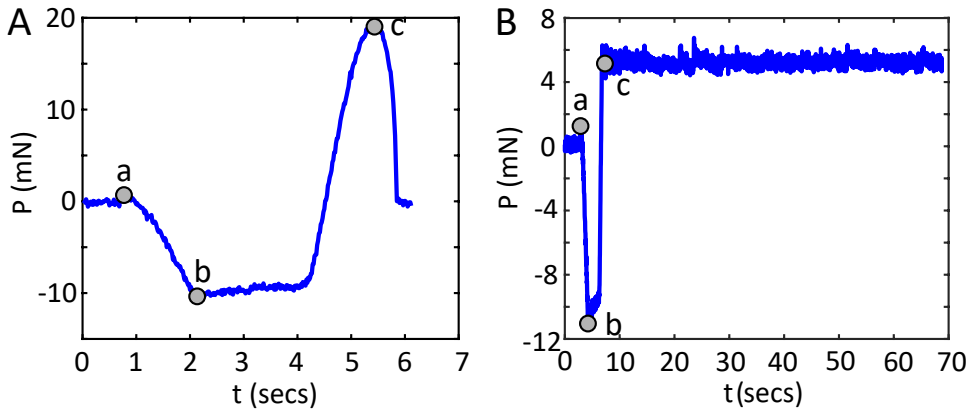

Figure 4.5: Example of the force experienced by a electroadhesive over time. A) The plot shows the force over time of a JKR tack test without an applied voltage. The loading phase (a) is when the probe approaches the glass slide at 6 µm until contact and a mechanical preload (b) of 10 mN. The probe is then unloaded until contact is broken at the tack force (c). B) The plot shows the force over time of a creep test where the electroadhesive is held at a force of 10 mN for at least 1 min. The electroadhesive is loaded at a speed of 3 µm/sec (a) to a set preload (b) and then immediately unloaded at 3 µm/sec to the set holding force (c). The small dips in force during the creep test is due to the linear stage displacing in order to keep a constant force.

the sample so that visually all bumps were in contact and had approximately the same contact radius at a given preload. For the devices with only a single bump, alignment was not as crucial since the surface had the same radius of curvature and some misalignment did not cause the contact area to be significantly different.

Textured EAs that were tested for the pull-in effect were plasma bonded to the ITO glass slide to prevent the bottom side from delaminating during the tack test. The plasma wand, Corona SB from Elveflow, was used to treat the bottom surface of the electroadhesive and the ITO glass slide. The two surfaces were pressed together and heated on a hot plate at 90 °C for at least 2 min. For all other experiments, the samples were pressed onto the ITO slide without plasma bonding.

Creep tests were conducted to obtain the holding force of the electroadhesives. The preloads were the same as in the tack tests, and the loading speed was 3 µm/sec and the unloading speed was 3 µm/sec. A feedback loop was used on the linear stages to maintain a constant force by changing displacement until adhesion failed. If the electroadhesive was able to maintain contact for a minimum of 1 min before failure, then that force was considered to be the maximum holding force, P_h. This was conducted at voltages ranging from 0 V to 400 V at a 100 V increments.

The potential use of textured EAs for pick and place applications was demonstrated by mounting them onto 3D printed parts and picking up various objects. The 3D printed parts were made by the Objet30 Pro for manual handling and for mounting the device to a robotic arm, Fig. 4.6.

The 3x3 textured EAs were used to pick up objects with weights from 2 g to 60 g. A 4x4 bump array was attached to the Kuka LBR iiwa through 3D printed

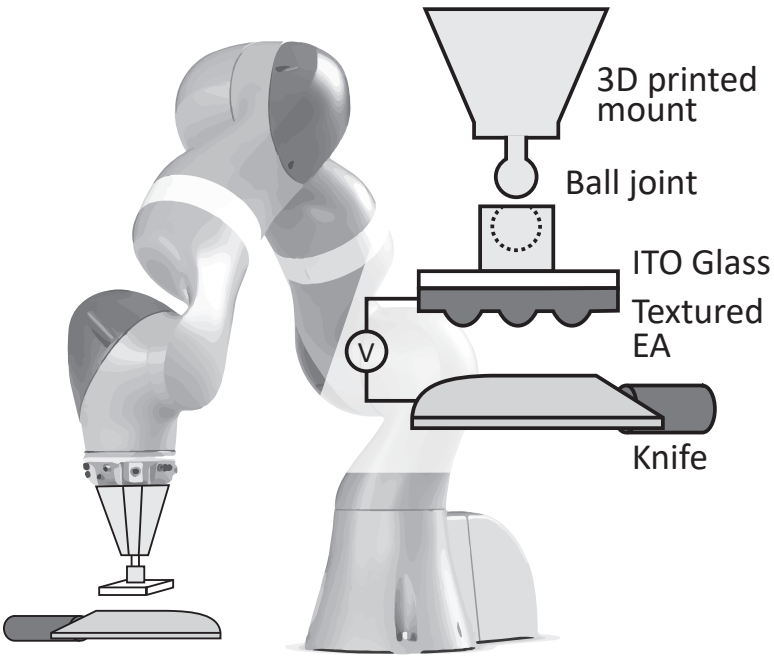

Figure 4.6: Image of a Kuka arm with a textured electroadhesive mounted onto a 3D printed part.

parts. It was mounted on a ball joint in order to allow the textured device to easily align its surface to the knife without having to adjust the angle of the robot arm. The weight of the knife was 60 g.

4.3 Results and Discussion

4.3.1 Single Bump

To show that Eqn. 4.3 can predict the contribution of electrostatics to tack force, tack tests were performed on bumps with three radius of curvatures: 7, 11, and 30 mm. Fig. 4.7 shows the electrostatic contribution to tack force plotted against voltage squared, for bumps with different radius of curvatures. The nominal tack force at zero voltage, P_o, was subtracted out of the total tack force, P_c, to obtain the

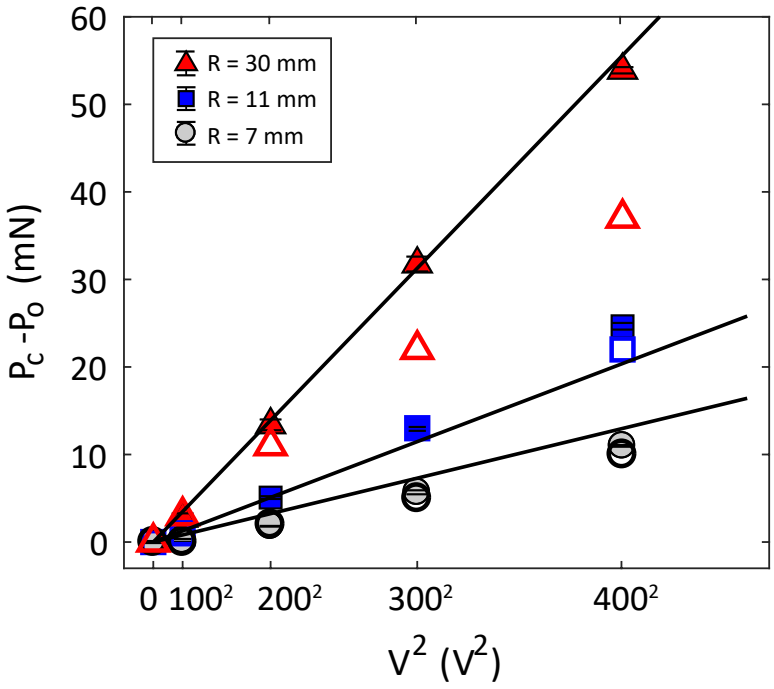

Figure 4.7: Electrostatic tack force plotted against the applied voltage squared for conductive polymeric spherical surfaces contacting a rigid ITO glass slide. The theory line is based on Eqn. 4.3, the solid markers indicate the electrostatic contribution to tack force, and the hollow markers, the holding force.

electrostatic force, P_v, solid colored markers. This was similarly done with the creep tests that measured the holding force, indicated by the unfilled markers. Eqn. 4.3, plotted as solid lines, predicts the electrostatic force between a sphere, with a radius of curvature, R, separated by a distance, d, from a conductive plate. In Fig. 4.1 the distance, d, was replaced by the dielectric thickness of the PDMS, 6 µm, and the measured radius and applied voltage was used for R and V, respectively. Constants were not used to modify the theoretical force. The tack forces, filled markers, were an average of at least 3 tack tests done at each applied voltage. The holding forces, unfilled markers, were the maximum forces that could be maintained for at least 1 min for each applied voltage.

Fig. 4.7 demonstrates that Eqn. 4.3 can predict the electrostatic contribution to tack force and the holding force of spherical bumps with radii lower than 10 mm. This will help inform the design of bump arrays and how it affects the controllable adhesion range of electroadhesive devices. As the radius of curvature increased beyond 10 mm, the holding force did not increase at the same rate. For the bump with a radius of 30 mm, the holding force was lower than the tack force by an average of 30% across all the applied voltages. The large discrepancy may be due to the spherical bump not having a uniform curvature. This variation in the curvature, caused by the fabrication process, creates an irregular stress distribution and can cause failure to occur earlier than predicted. Non-uniformity in the curvature was a result of using a milling machine to make the molds. External sources of error, such as, vibration of the acrylic plate during milling, quality of the end mills, the cutting path used by the program, contributed to discrepancies in the desired and actual dimensions.

4.3.2 Bump Array

Fig. 4.8 shows the electrostatic force plotted against voltage squared for textured electroadhesives. The nominal tack force at zero voltage was subtracted from the total tack force to obtain the electrostatic force. Four different arrays were tested: 1, 4, 9, 16, and 25 bumps. The distance between each bump was fixed at 3 mm so as the number of bumps increased so did the size of the device, from 36 mm^2 to 225 mm^2. Tack tests were conducted with voltages from 0 V to 300 V in 100 V increments. The markers indicate an average of at least 3 trials done at each voltage. The loading and

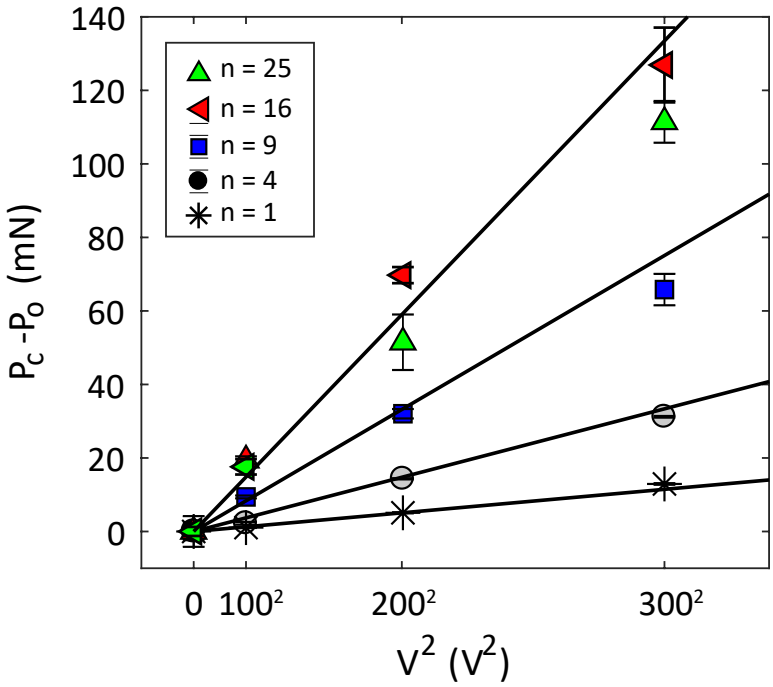

Figure 4.8: Electrostatic tack force plotted against the applied voltage squared for textured electroadhesives contacting a rigid ITO glass slide. The theory line is based on Eqn. 4.5 and the radius of curvature was 8 mm.

unloading speeds were the same as in the single bump tack tests.

The preload applied to the arrays depended on the number of bumps. It was set so that a 10 mN preload was applied for each bump in the array, e.g. a 3x3 bump array had a preload of 90 mN. The solid lines indicate the predicted electrostatic force based on Eqn. 4.5. The radius of curvature was 8 mm, dielectric thickness, 6 µm, and the dielectric constant, 2.5. The arrays with 16 or less bumps performed as predicted with Eqn. 4.5. However, for the textured device with 25 bumps, green triangles, it performed worst than the 16 bump textured device.

The holding force of the textured devices was also tested from 0 V to 300 V in 100 V increments, as shown in Fig. 4.9. The solid line is Eqn. 4.5 subtracted by the nominal tack force plotted as a function of voltage squared. For arrays with 16

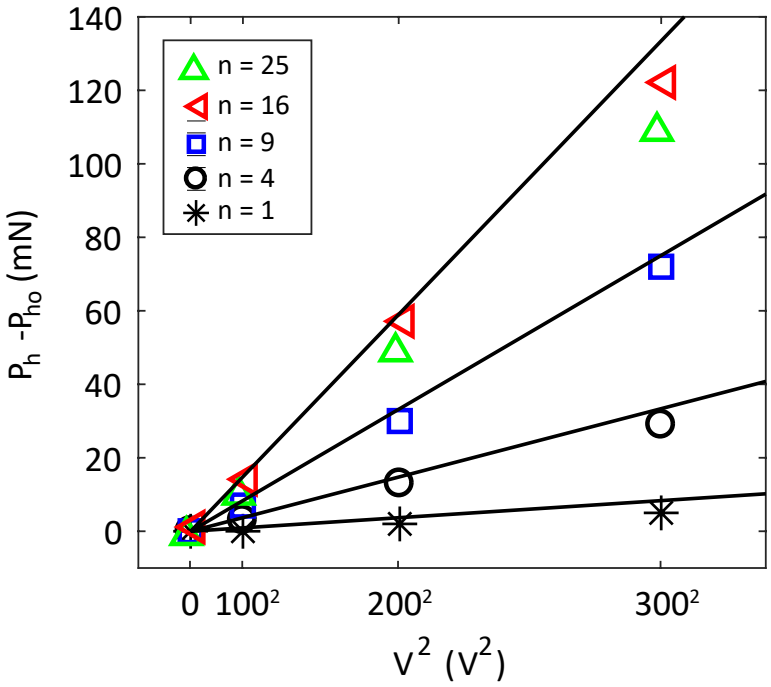

Figure 4.9: Electrostatic holding force plotted against the applied voltage squared in textured electroadhesives. The theory line is based on Eqn. 4.5 and the radius of curvature was 8 mm.

bumps or less, the tack force and holding force due to electrostatic matched well with the theory. However, similarly in the Fig. 4.8, the 25 bump array, green triangles, performed worst than the 16 bump array. This was due to imprecision in the milling process which resulted in certain bumps that did not have the same height as the majority. This caused the shorter bumps to have a smaller contact radius for a fixed preload and, therefore, a lower contribution to tack force.

Fig. 4.10 shows an array of 25 bumps at various points during the unloading phase. It can be seen that a section of bumps in the middle of the device were not as in contact with the surface as the rest of the bumps. And these bumps actually detached earlier in the unloading phase before the tack force was reached. Additional error can also occur due to misalignment of the contacting surfaces. Misalignment

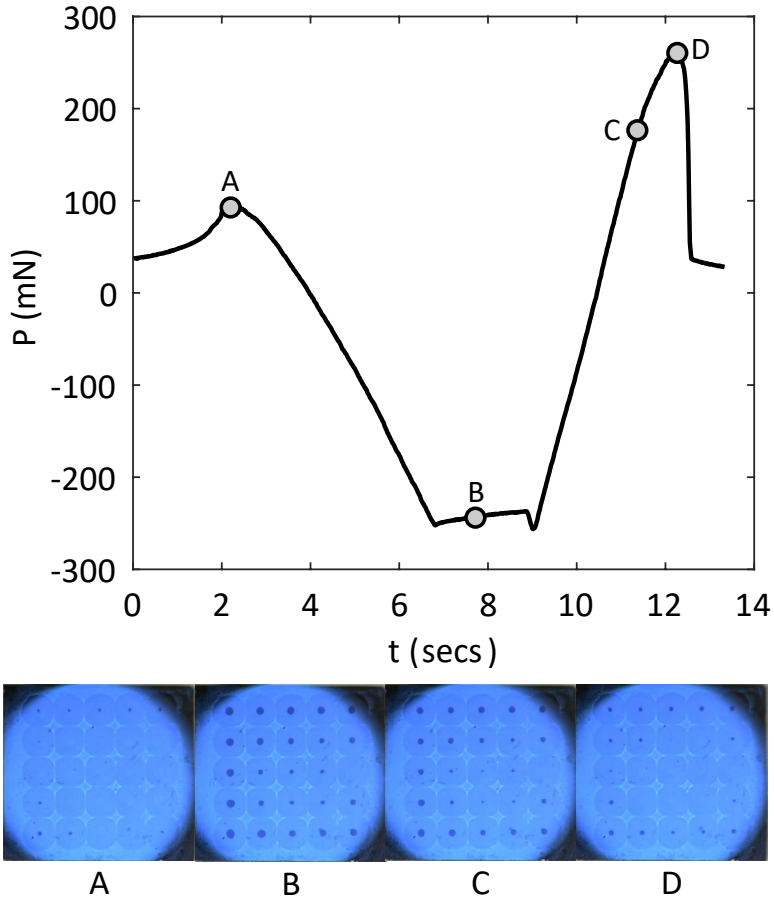

Figure 4.10: Example of a tack test for the textured electroadhesive with $n = 25$. The inserted image shows that the middle bumps where not as in contact as the others and that they detached earlier during the unloading phase, before reaching the tack force.

causes certain sides of the array to be in more contact than the opposite side, resulting in a lower tack force than if the surfaces were perfectly aligned.

Despite some limitations in fabrications, it can be seen from Fig. 4.8 and Fig. 4.9 that the controllable adhesion range increases linearly with the number of bumps in a textured device. And given that the nominal adhesion of bump arrays increases at a rate of $n^{1/2}$, the normalized adhesion range can be increased by simply adding more bumps. However, to continue the increase for larger arrays it is necessary to improved the fabrication process so that the mold's dimensions do not vary as much. Another

conclusion is that while the radius of curvature may affect the maximum adhesion, it does not affect the adhesion range based on Eqn. 4.6. Bumps with smaller radius of curvature could then be used to densely pack an area, while achieving a larger adhesion range.

4.3.3 Multi-tiered areas

Another method of increasing the adhesion range is to design multi-tiered contact areas, which are separated by height, where for different applied loads different contact areas are reached. Fig. 4.2 shows a schematic of a two tiered device, where the first tier is a bump that first comes into contact with the surface, and the second tier is the plane around the bump which will contact the surface if enough load is applied to the device. This load can be mechanically or electrostatically applied. By having contact areas at different heights, the controllable adhesion range can be changed based on the contact area of the first and second tier. Fig. 4.11 demonstrates the performance of a multi-tiered 3x3 bump array, where the first tier was a set of 9 bumps and the second tier was the area around the bumps, totaling 72 mm^2. The radius of curvature and height of the bumps was 8 mm and 15 µm. With only the first tier area in contact, shown in the insert of Fig. 4.11, the device performed like the textured devices in Fig. 4.8, following Eqn. 4.5. The device's performance however, jumps dramatically when the second tier area is engaged at voltages above 160 V. The maximum electrostatic force that was observed was 2.8 N at 300 V. The theory line was calculated using the electrostatic parllel plate model, Eqn. 4.7 modified by a

constant $c = 0.5$.

Each point is a tack test performed with an applied voltage, and the red x markers at 0 V indicate the nominal tack force for when the second tier area is in contact with a preload of 600 mN. The jump in tack forces in-between 150 V and 160 V was due to the second tier area pulling in and contacting the attachment surface. The large change in P_c is due to an incomplete pull-in of the area with only a portion in contact. This partial contact is due to the second tier having an uneven surface, such that, the electrostatic force is not as strong in certain areas. However with a large enough voltage, in this case, larger than 160 V, the second tier area can be brought into nearly full contact with the attachment surface, and the increase in tack force stablizes and follows the trend described by the parallel plate model.

The pull-in voltage depends on the amount of mechanical preload that is applied, the higher the preload, the lower the pull-in voltage. At higher preloads the gap between the contacting surface and the second tier area is smaller, and thus, requires less electrostatic force to close the gap. However, if the preload is too small, pull-in will not occur since the gap is too large for the electrostatic force to close.

During pull-in, air bubbles may be trapped between the two interfaces, as shown in the insert in Fig. 4.12. This is due to an uneven and random collapse of the gaps between the surface and adhesive. Surface roughness and misalignment can cause varying gaps between the interfaces. The collapsed bumps also deform the surface around them which prevent contact from occuring. While the jump between the electroadhesion range, 0 mN to 0.1 mN and 2 N to 3 N, is large, this jump can be easily adjusted by changing the range of the first tier through varying the numbers

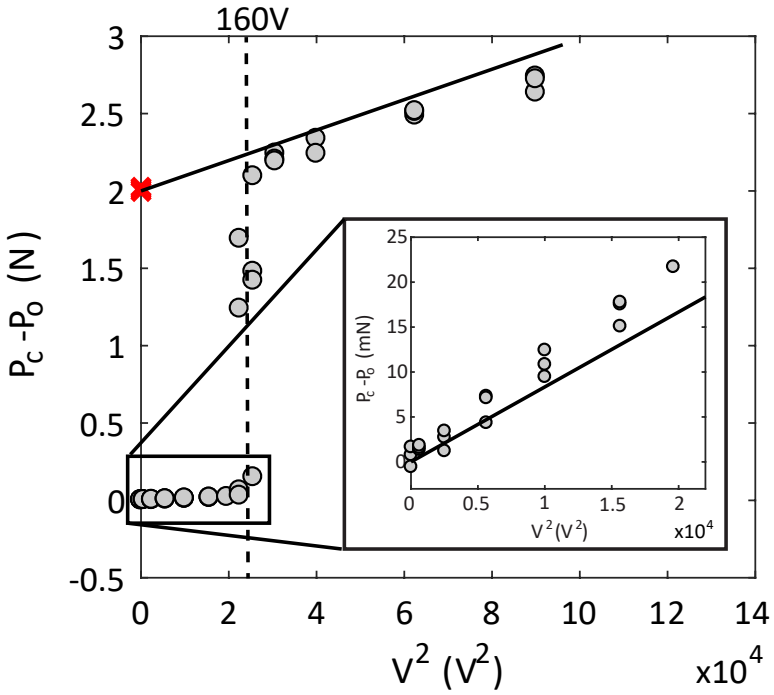

Figure 4.11: Electrostatic tack force plotted against applied voltage squared for a 3x3 textured device with a preload of 225 mN. The black theory line in the insert is based on Eqn. 4.5, and shows that the electrostatic tack force matches well. The trend line in the main figure is the electrostatic force for parallel plates, Eqn. 4.7, with a constant $c = 0.5$ to fit the tack forces. The pull-in voltage was approximately 160 V.

of bumps or changing the area of the second tier. The second tier area could be modified by adjusting the overall dimensions of the device or replacing it with flat pillars in between each bump. Flat pillars with defined contact areas as the second tier can reduce the presence of air bubbles by limiting the effect of the stress from the compressed bumps, and can be easily used to control the total 2nd tier area.

4.3.3.1 Adhesion hystersis

In addition to varying the voltage between experiments, the benefit of using electrostatic force is the ability to freely adjust adhesion during an experiment. Fig. 4.12 shows a 3x3 textured device being stepped between 0 V and 400 V at 10 V increments over time. For Fig. 4.12A the device was first preloaded to 10 mN and allowed to relax for at least 2 min. There was approximately a 6 sec wait between each voltage step to allow the polymer to relax. The change in electrostatic force at higher voltages was larger than at lower voltages because electrostatic force is related to voltage squared. This active change in adhesion can be cycled multiple times without degradation in the adhesive force, as shown in Fig. 4.13.

In Fig. 4.12B, the device was preloaded to 100 mN and allowed to relax for at least 2 min, then an applied voltage was stepped from 0 V to 400 V and back down at 10 V increments. Pull-in occurred at 350 V, however, as the voltage was stepped back down, the pulled-in area did not detach. This is because the mechanically stored force in the cantilever beam was not large enough to overcome the nominal adhesion of the second tier area. This adhesive hysteresis is one main drawback to this specific design

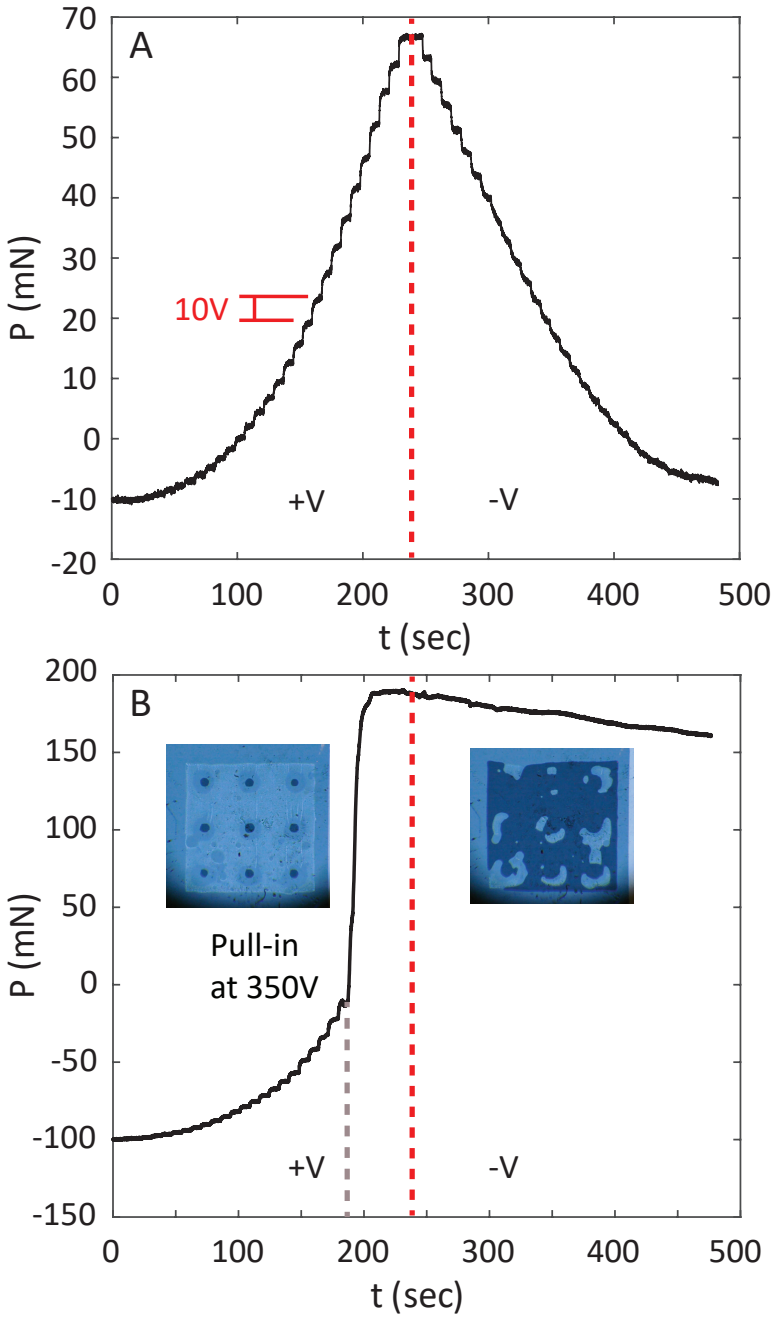

Figure 4.12: Electroadhesion experienced by a 3x3 textured device plotted against time. Each step in load corresponded to a 10 V step in applied voltage; the voltage was stepped from 0 V to 400 V and back down, with approximately 6 sec in between each step. A) The device was preloaded to 10 mN and allowed to relax for at least 2 min before stepping the voltage. B) The device was preloaded to 100 mN and allowed to relax for at least 2 min before stepping the voltage. The textured electroadhesive pulled-in at 350 V, as shown by the large increase in load.

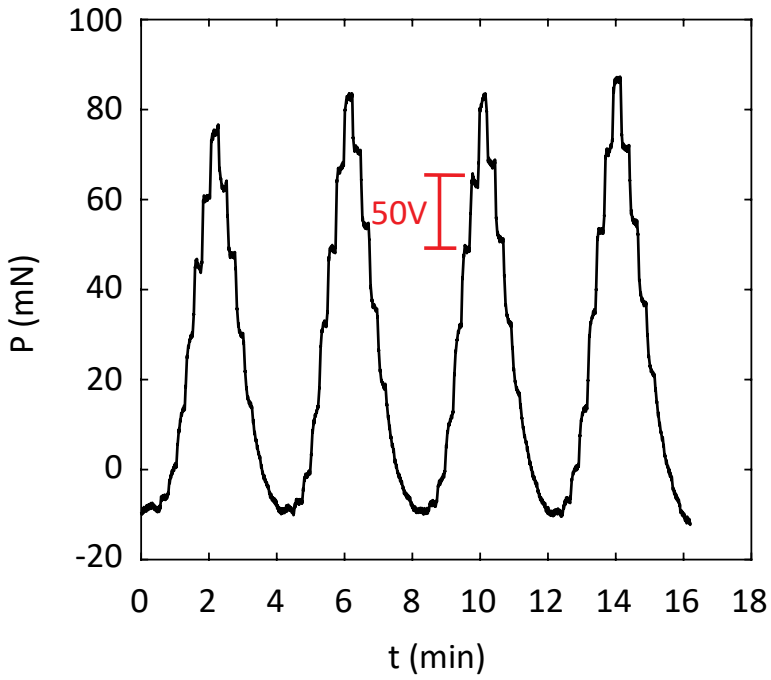

Figure 4.13: Electroadhesion experienced by a 3x3 textured device plotted against time, demonstrating the ability to step up and down voltage multiple times. The device was preloaded to 10 mN before beginning the experiment. The voltage was stepped from 0 V to 400 V in 50 V increments and back down, with approximately 15 sec in between each step.

since once the second tier area is in contact it requires a large detachment force to remove the sample from the attachment surface and cannot be cycled like in Fig. 4.13. Fig. 4.13 shows a 3x3 textured device with a preload of 10 mN being stepped up to 400 V and back down to 0 V at 50 V increments. There was a 15 sec wait inbetween each voltage step. With only the first tier area in contact, the textured electroadhesive can be cycled between 0 V and 400 V without any degradation in adhesion.

4.3.4 Applications

To demonstrate the application of textured electroadhesives in pick and place, the devices were mounted onto 3D printed devices and used to pick up various everyday

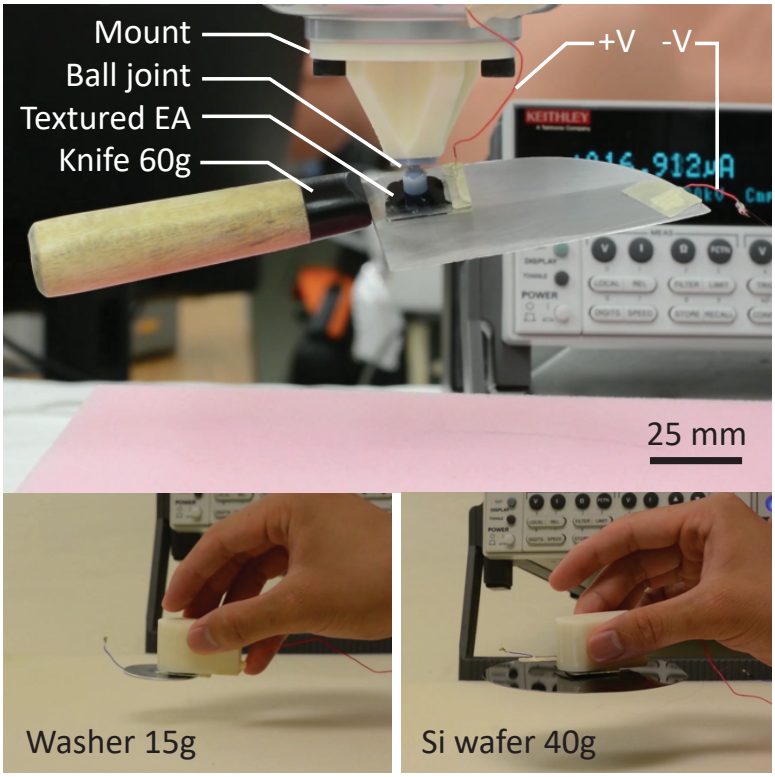

Figure 4.14: Images of a 3x3 textured electroadhesive picking up a knife using a Kuka arm with 300 V. The Si wafer and steel washer was manually picked up with an applied voltage of 120 V and 200 V, respectively.

objects. Four objects with varying weights and surface roughness were used: razor blades, a steel washer, silicon wafer, and kitchen knife. All of the objects were metallic and had a metal wire connected to their surface to apply a voltage between them and the textured electroadhesive. The mass of the objects ranged from 2 g to 60 g. These objects were manually picked up by hand and required different preloads in order to pick them up. For the razor blades, steel washer, and silicon wafer the preload was the weight of the 3D printed handle and the textured device. This was so that only the first tiered area was in contact when the voltage was applied. This is necessary since if the second tier area was in contact then the objects would not detach after the electroadhesion was turned off. This is because the nominal holding

force of the second tier area was approximately 0.3 N (30 g), which means any lighter objects would permanently stay attached to the device even without electrostatic force. For the knife, the textured device had to be pressed into the object with force to ensure that pull-in occurs, such that, the second tier area was engaged. The nominal holding force was less than the weight of the heavier objects but by applying 300 V the electroadhesion was large enough to be able to hold the knife.

After turning off the voltage, the objects did not immediately detach, it took them on average 2-5 secs. This is because it takes some time for the crack to propagate through the contact area and there is some residual charge left between the interfaces.

A robotic arm from Kuka was used to demonstrate pick and place for a 4x4 bump array picking up a knife that weighs 60 g, shown in Fig. 4.14. The robot arm was position controlled and had no force feedback. The position was manually picked so that it could provide a sufficient preload such that without a voltage the knife would not stick to the electroadhesive, but with an applied voltage it would stick. The surface was a pink foam to prevent damaging the knife during testing. A ball joint was necessary to help the electroadhesive passively align its surface to the knife's metal surface. Without a passive method of aligning the two surfaces, it would be difficult and time consuming to actively control the angle of the robot arm so that the two surfaces were parallel. The electroadhesive was manually positioned so that it would press down on the center of mass of the knife to pick it up.

In real world applications a target object for picking up will not be electrically connected to the electroadhesive. Instead interdigitated electroades would be used to pick up conductive and non-conductive objects. While this work does not explore

interdigitated electrode design, the design framework and fabrication process put forth in this paper can be easily adapted to interdigitated designs.

Chapter 5

Conclusion

5.1 Contributions

This work in electroadhesion has led to a basic friction model that can estimate the critical shear adhesion of an all-polymer electroadhesive, an adaptation to the JKR theory to include the effect of electrostatic force on crack propagation, and a design framework that combines dry and electroadhesives while lowering the required voltage and increasing the range of controllable adhesion. The primary contributions of this work are summarized as follows:

- Basic friction model that estimates the critical shear strength of an all-polymer electroadhesive
- Stiff dielectric layers improve adhesion due to dissipating energy from crack propagation
- Theory and experiments that characterize electrostatic force in terms of critical energy release rate
- Critical energy release rate can be described as a superposition of the polymer's inherent stickiness and electrostatic force
- The characteristic crack speed increases with applied voltage because the cohe-

sive zone increases with electrostatic force

- Fabrication technique that can easily create a large array of spherical bumps and deposit a thin 6 μm PDMS dielectric
- Electrostatic force exerted by a textured electroadhesive increases linearly with the number of spherical bumps
- Multi-tiered electroadhesive that can increase adhesion by up to 20x
- Demonstration of a Kuka arm picking up a metal knife with a textured electroadhesive

5.2 Published papers

- Abraham Simpson Chen, Alexi Charalambides, and Sarah Bergbreiter. High strength low voltage microfabricated electroadhesives on nonconductive surfaces. In *Hilton Head Solid-State Sensors, Actuators, and Microsystems Workshop*, Hilton Head Island, SC, June 2014.
- Abraham Simpson Chen and Sarah Bergbreiter. Electroadhesive feet for turning control in legged robots. In *Robotics and Automation (ICRA),2016 IEEE International Conference on* (pp. 3806-3812). IEEE, May 2016.
- Abraham Simpson Chen and Sarah Bergbreiter. A comparison of critical shear force in low-voltage, all-polymer electroadhesives to a basic friction model. *Smart Materials and Structures*, 26(2):025028, 2017.

5.3 Planned papers

- Simpson Abraham Chen, Christopher Barney, Alfred J. Crosby, and Sarah Bergbreiter. Characterizing the combined effect of electrostatic force and polymer adhesion in conductive elastomers.

- Simpson Abraham Chen, Christopher Barney, Alfred J. Crosby, and Sarah Bergbreiter. Textured electroadhesives that uses van der Waals and electrostatic force at low voltages to achieve large controllable adhesion.

5.4 Future work

Future work in this field will involve continual development in refining the fabrication method to improve consistency in dimensions for multi-tiered devices. Different multi-tiered patterns and shapes will be explored to understand how they affect the tack and holding force. Simulations will also be done to explore how these textured surfaces will affect the electric fields in interdigitated electrodes and to identify the optimal textured and interdigitated patterns. Future work will also focus on theoretical work in contact mechanics. JKR equations have been modified for different probe and contact shapes, such as, flat punches and cylinders in contact. Electrostatic force will be adapted into those JKR equations and verified.

Bibliography

[1] Jun Shintake, Samuel Rosset, Bryan Schubert, Dario Floreano, and Herbert Shea. Versatile Soft Grippers with Intrinsic Electroadhesion Based on Multifunctional Polymer Actuators. *Advanced Materials*, 28(2):231–238, January 2016.

[2] Kevin Bullis. This method of robotic pickup could stick. *MIT Technology Review*, Oct 2014.

[3] Evan Ackerman. Sri shows new 'taurus' bomb-defusing prototype at stanford robot block party. *IEEE Spectrum*, April 2011.

[4] Jurg Germann, Bryan Schubert, and Dario Floreano. Stretchable electroadhesion for soft robots. In *Intelligent Robots and Systems (IROS 2014), 2014 IEEE/RSJ International Conference on*, pages 3933–3938. Ieee, 2014.

[5] Werner Brockmann. Concept for energy-autarkic, autonomous climbing robots. In *Climbing and Walking Robots*, pages 107–114. Springer, 2006.

[6] A Gimenez, M Abderrahim, VM Padron, and C Balaguer. Adaptive control strategy of climbing robot for inspection applications in construction industry. In *Proc. of the 15th Triennial World Congress of the IFAC*, 2002.

[7] Markus Eich and T. Vogele. Design and control of a lightweight magnetic climbing robot for vessel inspection. In *Control & Automation (MED), 2011 19th Mediterranean Conference on*, pages 1200—-1205, 2011.

[8] Peter Ward and Dikai Liu. Design of a high capacity electro permanent magnetic adhesion for climbing robots. In *Robotics and Biomimetics (ROBIO), 2012 IEEE International Conference on*, pages 217—-222, 2012.

[9] Patrick Schoeneich, Frederic Rochat, Olivier Truong-Dat Nguyen, Roland Moser, and Francesco Mondada. TRIPILLAR: a miniature magnetic caterpillar climbing robot with plane transition ability. *Robotica*, 29(07):1075–1081, April 2011.

[10] Bryan Laulicht, Robert Langer, and Jeffrey M Karp. Quick-release medical tape. *Proceedings of the National Academy of Sciences*, 109(46):18803–18808, 2012.

[11] Yoshiaki Urahama. Effect of peel load on stringiness phenomena and peel speed of pressure-sensitive adhesive tape. *The Journal of Adhesion*, 31(1):47–58, 1989.

[12] D.L. Christensen, E.W. Hawkes, S.A. Suresh, K. Ladenheim, and M.R. Cutkosky. utugs: Enabling microrobots to deliver macro forces with controllable adhesives. In *Robotics and Automation (ICRA), 2015 IEEE International Conference on*, pages 4048–4055, May 2015.

[13] Michael P Murphy, Casey Kute, Yiğit Mengüç, and Metin Sitti. Waalbot ii: adhesion recovery and improved performance of a climbing robot using fibrillar adhesives. *The International Journal of Robotics Research*, 30(1):118–133, 2011.

[14] Ozgur Unver, Ali Uneri, Alper Aydemir, and Metin Sitti. Geckobot: a gecko inspired climbing robot using elastomer adhesives. In *Robotics and Automation, 2006. ICRA 2006. Proceedings 2006 IEEE International Conference on*, pages 2329–2335. IEEE, 2006.

[15] Yuanfeng Han, Hamidreza Marvi, and Metin Sitti. Fiberbot: A miniature crawling robot using a directional fibrillar pad. In *Robotics and Automation (ICRA), 2015 IEEE International Conference on*, pages 3122–3127. IEEE, 2015.

[16] Michael D Bartlett, Andrew B Croll, Daniel R King, Beth M Paret, Duncan J Irschick, and Alfred J Crosby. Looking beyond fibrillar features to scale gecko-like adhesion. *Advanced Materials*, 24(8):1078–1083, 2012.

[17] Marleen Kamperman, Elmar Kroner, Aranzazu del Campo, Robert M McMeeking, and Eduard Arzt. Functional adhesive surfaces with "gecko" effect: The concept of contact splitting. *Advanced Engineering Materials*, 12(5):335–348, 2010.

[18] Maurizio Micciché, Eduard Arzt, and Elmar Kroner. Single macroscopic pillars as model system for bioinspired adhesives: Influence of tip dimension, aspect ratio, and tilt angle. *ACS Applied Materials & Interfaces*, 6(10):7076–7083, 2014. PMID: 24779439.

[19] M. Varenberg, A. Peressadko, S. Gorb, and E. Arzt. Effect of real contact geometry on adhesion. *Applied Physics Letters*, 89(12):121905, 2006.

[20] A. S. Chen and S. Bergbreiter. Electroadhesive feet for turning control in legged robots. In *2016 IEEE International Conference on Robotics and Automation (ICRA)*, pages 3806–3812, May 2016.

[21] Jeffrey M Karp and Robert Langer. Dry solution to a sticky problem. *Nature*, 477(7362):42, 2011.

[22] H. Prahlad, R. Pelrine, S. Stanford, J. Marlow, and R. Kornbluh. Electroadhesive robots x2014;wall climbing robots enabled by a novel, robust, and electrically controllable adhesion technology. In *2008 IEEE International Conference on Robotics and Automation*, pages 3028–3033, May 2008.

[23] Rui Chen. A gecko-inspired electroadhesive wall-climbing robot. *Potentials, IEEE*, 34(2):15–19, 2015.

[24] Stuart Diller, Carmel Majidi, and Steven H Collins. A lightweight, low-power electroadhesive clutch and spring for exoskeleton actuation. In *IEEE International Conference on Robotics and Automation*, 2016.

[25] M. A. Graule, P. Chirarattananon, S. B. Fuller, N. T. Jafferis, K. Y. Ma, M. Spenko, R. Kornbluh, and R. J. Wood. Perching and takeoff of a robotic insect on overhangs using switchable electrostatic adhesion. *Science*, 352(6288):978–982, May 2016.

[26] Donald Ruffatto, Jainam Shah, and Matthew Spenko. Optimization of electrostatic adhesives for robotic climbing and manipulation. In *ASME 2012 International Design Engineering Technical Conferences and Computers and Information in Engineering Conference*, pages 1143–1152. American Society of Mechanical Engineers, 2012.

[27] Donald Ruffatto, Aaron Parness, and Matthew Spenko. Improving controllable adhesion on both rough and smooth surfaces with a hybrid electrostatic/gecko-like adhesive. *Journal of The Royal Society Interface*, 11(93):20131089, 2014.

[28] K. Asano, F. Hatakeyama, and K. Yatsuzuka. Fundamental study of an electrostatic chuck for silicon wafer handling. *IEEE Transactions on Industry Applications*, 38(3):840–845, May 2002.

[29] A. Simpson Chen, Alexi Charalambides, and Sarah Bergbreiter. High strength, low voltage microfabricated electroadhesives on nonconductive surfaces. In *Hilton Head Solid-State Sensors, Actuators, and Microsystems Workshop*, Hilton Head Island, SC, June 2014.

[30] Juan P Díaz Téllez, Jeff Krahn, and Carlo Menon. Characterization of electroadhesives for robotic applications. In *Robotics and Biomimetics (ROBIO), 2011 IEEE International Conference on*, pages 1867–1872. IEEE, 2011.

[31] Jose Berengueres, Masataka Urago, Shigeki Saito, Kenjiro Tadakuma, and Hiroyuki Meguro. Gecko inspired electrostatic chuck. In *Robotics and Biomimetics, 2006. ROBIO'06. IEEE International Conference on*, pages 1018–1023. IEEE, 2006.

[32] Jeffrey Krahn and Carlo Menon. Electro-dry-adhesion. *Langmuir*, 28(12):5438–5443, 2012.

[33] Hadi Izadi, Katherine M. E. Stewart, and Alexander Penlidis. Role of contact electrification and electrostatic interactions in gecko adhesion. *Journal of The Royal Society Interface*, 11(98), 2014.

[34] Hadi Izadi and Alexander Penlidis. Polymeric bio-inspired dry adhesives: Van der waals or electrostatic interactions? *Macromolecular Reaction Engineering*, 7(11):588–608, 2013.

[35] Alfred J. Crosby, Kenneth R. Shull, Hamed Lakrout, and Costantino Creton. Deformation and failure modes of adhesively bonded elastic layers. *Journal of Applied Physics*, 88(5):2956, 2000.

[36] Kenneth Shull. Contact mechanics and the adhesion of soft solids. *Materials Science and Engineering: R: Reports*, 36(1):1 – 45, 2002.

[37] Kenneth R. Shull, Dongchan Ahn, Wan-Lin Chen, Cynthia M. Flanigan, and Alfred J. Crosby. Axisymmetric adhesion tests of soft materials. *Macromolecular Chemistry and Physics*, 199(4):489–511, 1998.

[38] M. Barquins and D. Maugis. Tackiness of elastomers. *The Journal of Adhesion*, 13(1):53–65, 1981.

[39] KL Johnson, K Kendall, and AD Roberts. Surface energy and the contact of elastic solids. In *Proceedings of the Royal Society of London A: Mathematical, Physical and Engineering Sciences*, volume 324, pages 301–313. The Royal Society, 1971.

[40] Aaron Parness, Daniel Soto, Noé Esparza, Nick Gravish, Matt Wilkinson, Kellar Autumn, and Mark Cutkosky. A microfabricated wedge-shaped adhesive array displaying gecko-like dynamic adhesion, directionality and long lifetime. *Journal of the Royal Society Interface*, pages rsif–2009, 2009.

[41] Brigitte Temple, Aiva Simaite, and Matthew Spenko. The effect of bending compliance on adhesion pressure of hybrid electrostatic/gecko-like adhesives. In *2018 IEEE International Conference on Robotics and Automation (ICRA)*, pages 6773–6778. IEEE, 2018.

[42] Keng Huat Koh, M Sreekumar, and SG Ponnambalam. Hybrid electrostatic and elastomer adhesion mechanism for wall climbing robot. *Mechatronics*, 35:122–135, 2016.

[43] JM Krahn, AG Pattantyus-Abraham, and C Menon. Polymeric electro-dry-adhesives for use on conducting surfaces. *Proceedings of the Institution of Mechanical Engineers, Part L: Journal of Materials: Design and Applications*, 228(2):109–114, 2014.

[44] Abraham Simpson Chen and Sarah Bergbreiter. A comparison of critical shear force in low-voltage, all-polymer electroadhesives to a basic friction model. *Smart Materials and Structures*, 26(2):025028, 2017.

[45] Hua Shen, Rong Liu, Rui Chen, and Junhu He. Modeling of attraction force generated by interdigital electrodes for electroadhesive robots. pages 678–681. IEEE, July 2012.

[46] Jeonghoon Yoo, Jae-Seok Choi, Sang-Joon Hong, Tae-Hyun Kim, and Sung Jin Lee. Finite element analysis of the attractive force on a coulomb type electrostatic chuck. In *Electrical Machines and Systems, 2007. ICEMS. International Conference on*, pages 1371–1375. IEEE, 2007.

[47] AD Crocombe. Global yielding as a failure criterion for bonded joints. *International Journal of Adhesion and Adhesives*, 9(3):145–153, 1989.

[48] L. Leger and C. Creton. Adhesion mechanisms at soft polymer interfaces. *Philosophical Transactions of the Royal Society A: Mathematical, Physical and Engineering Sciences*, 366(1869):1425–1442, April 2008.

[49] Ivan Penskiy, Aaron P Gerratt, and Sarah Bergbreiter. Friction, adhesion, and wear properties of pdms coatings in mems devices. In *Micro Electro Mechanical Systems (MEMS), 2011 IEEE 24th International Conference on*, pages 440–444. IEEE, 2011.

[50] Specialty Coating Systems. *SCS Parylene Properties*, 2007.

[51] DuPont Teijin Films. *"Mylar Polyester Film: Electrical Properties*, 4 2003.

[52] Aaron P Gerratt and Sarah Bergbreiter. Dielectric breakdown of pdms thin films. *Journal of Micromechanics and Microengineering*, 23(6):067001, 2013.

[53] Michael D. Bartlett, Andrew B. Croll, and Alfred J. Crosby. Designing Bio-Inspired Adhesives for Shear Loading: From Simple Structures to Complex Patterns. *Advanced Functional Materials*, 22(23):4985–4992, December 2012.

[54] Alexi Charalambides and Sarah Bergbreiter. A novel all-elastomer mems tactile sensor for high dynamic range shear and normal force sensing. *Journal of Micromechanics and Microengineering*, 25(9):095009, 2015.

[55] Michael D. Bartlett and Alfred J. Crosby. Scaling Normal Adhesion Force Capacity with a Generalized Parameter. *Langmuir*, 29(35):11022–11027, September 2013.

[56] Daniel R King, Michael D Bartlett, Casey A Gilman, Duncan J Irschick, and Alfred J Crosby. Creating gecko-like adhesives for "real world" surfaces. *Advanced Materials*, 26(25):4345–4351, 2014.

[57] Seok Kim, Metin Sitti, Chung-Yuen Hui, Rong Long, and Anand Jagota. Effect of backing layer thickness on adhesion of single-level elastomer fiber arrays. *Applied Physics Letters*, 91(16):161905, 2007.

[58] Lucas FM da Silva, TNSS Rodrigues, MAV Figueiredo, MFSF De Moura, and JAG Chousal. Effect of adhesive type and thickness on the lap shear strength. *The journal of adhesion*, 82(11):1091–1115, 2006.

[59] Yoshihide Fukahori and Hirotaka Yamazaki. Mechanism of rubber abrasion: Part 2. general rule in abrasion pattern formation in rubber-like materials. *Wear*, 178(1):109–116, 1994.

[60] Michel Barquins. Sliding friction of rubber and schallamach waves—a review. *Materials science and engineering*, 73:45–63, 1985.

[61] GJ Lake and A Stevenson. Wave phenomena in low angle peeling. *The Journal of Adhesion*, 12(1):13–22, 1981.

[62] Bi-min Zhang Newby and Manoj K Chaudhury. Friction in adhesion. *Langmuir*, 14(17):4865–4872, 1998.

[63] Abel L Thangawng, Rodney S Ruoff, Melody A Swartz, and Matthew R Glucksberg. An ultra-thin pdms membrane as a bio/micro–nano interface: fabrication and characterization. *Biomedical microdevices*, 9(4):587–595, 2007.

[64] Rong Liu, Rui Chen, Hua Shen, and Rong Zhang. Wall climbing robot using electrostatic adhesion force generated by flexible interdigital electrodes. *International Journal of Advanced Robotic Systems*, page 1, 2013.

[65] Mathew Barton, John W. Morley, Marcus A. Stoodley, Kheng-Seong Ng, Sabine C. Piller, Hong Duong, Damia Mawad, David A. Mahns, and Antonio Lauto. Laser-activated adhesive films for sutureless median nerve anastomosis. *Journal of Biophotonics*, 6(11-12):938–949.

[66] Christian Heinzmann, Souleymane Coulibaly, Anita Roulin, Gina L. Fiore, and Christoph Weder. Light-induced bonding and debonding with supramolecular adhesives. *ACS Applied Materials & Interfaces*, 6(7):4713–4719, 2014. PMID: 24484360.

[67] Xiaofan Luo, Kathryn E. Lauber, and Patrick T. Mather. A thermally responsive, rigid, and reversible adhesive. *Polymer*, 51(5):1169 – 1175, 2010.

[68] Minh Khanh Nguyen, Cong Truc Huynh, and Doo Sung Lee. ph-sensitive and bioadhesive poly(-amino ester)–poly(ethylene glycol)–poly(b-amino ester) triblock copolymer hydrogels with potential for drug delivery in oral mucosal surfaces. *Polymer*, 50(22):5205 – 5210, 2009.

[69] Dan A Hays. Role of electrostatics in adhesion. In *Fundamentals of Adhesion*, pages 249–278. Springer, 1991.

[70] Tian Tang, Chung-Yuen Hui, and Anand Jagota. Adhesive contact driven by electrostatic forces. *Journal of Applied Physics*, 99(5):054906, 2006.

[71] Joseph M Crowley. Simple expressions for force and capacitance for a conductive sphere near a conductive wall. In *Proceedings of the ESA Annual Meeting on Electrostatics*, page 1, 2008.

[72] Jeffrey Krahn and Carlo Menon. Electro-dry-adhesion. *Langmuir*, 28(12):5438–5443, 2012.